MSc. Thesis Biomedical Engineering

faculty of Science and Technology
Biomedical Photonic Imaging

Combined Optical Coherence Tomography and Imaging Single Fiber Reflectance Spectroscopy

Overcoming the problem of glare in order to realize quantitative
spectral measurements in a novel combined endoscopic system

Author:
R. van Zutphen

Supervisors:
Dr. ir. X. Attendu
Prof. Dr. Ir. N. Bosschaart
Dr. Ir. C.A. Cuartas Velez
Prof. Dr. Ir. R.M. Verdaasdonk
Prof. Dr. Ir. T.G. van Leeuwen

May 5, 2024

UNIVERSITY
OF TWENTE.

Amsterdam UMC

Abstract

Optical Coherence Tomography (OCT) has increasingly been recognized for its potential across various medical imaging applications. However, it is often considered not quite ready for full clinical integration. Particularly in cancer detection, while OCT has shown promising results, a multimodal approach could potentially yield more comprehensive diagnostics and accelerate its clinical translation. This thesis explores a method to mitigate the challenge of unwanted reflections, or glare, during the acquisition of co-registered spectral information through a novel technique known as imaging single fiber reflectance spectroscopy (iSFR), which is a prime candidate for multimodal OCT.

Initially, we employ Monte Carlo (MC) simulations to assess the feasibility of extending current models to iSFR geometries to correlate measured reflectance spectra to tissue optical properties. However, the conversion of existing models proves inaccurate due to the increased ballistic nature of photons in iSFR. We hypothesize that a future iSFR model may exhibit nonlinear behavior similar to the current SFR models and, therefore, explore the potential for glare incorporation within an SFR framework. Our findings demonstrate that by modeling glare as Fresnel reflections, it is possible to decouple glare from the desired signal with a signal-to-noise Ratio (SNR) up to 15 dB, which indicates that it may be possible to incorporate glare as additional optimization parameters in future iSFR models.

Furthermore, we evaluate the developed algorithm's efficacy within a benchtop OCT/iSFR system, focusing on distinguishing glare from the actual reflective spectra of homogeneous samples that did not require a model. The algorithm struggled to accurately characterize the spectral shape of glare, which we ascribe to several issues, with poor data quality being the predominant factor.

Lastly, a preliminary study was conducted to determine whether specific OCT signal characteristics, such as intensity ratios and speckle patterns, could indicate the amount of glare present in iSFR. It became evident that establishing such a relationship would require more time than was available, as we identified the need for a more robust measurement protocol and additional considerations when comparing these two modalities. Despite the inconclusive results, it does pave the way for future work. It not only provided new insights into the integration of both modalities but also led to a novel method for measuring the length of optical fibers.

Overall, our research demonstrated that it is possible to include glare as several fitting parameters in SFR models, indicating the potential of developing iSFR models for quantitative reflective analysis. We also established a framework to simulate a large number of MC simulations for this development and identified areas for improvement and considerations for future model development.

Abbreviations

AI	Artificial Intelligence
APC	Angled Physical Contact
AWG	Arbitrary Waveform Generator
BD	Beam Dump
BPF	Band Pass Filter
CPSF	Confocal Point Spread Function
CR	Circulator
CT	Computed Tomography
DCF	Double Clad Fiber
DCFC	Double Clad Fiber Coupler
DRS	Diffuse Reflectance Spectroscopy
EC	Esophageal Cancer
FBG	Fiber Bragg Grating
FD	Fourier Domain
GPU	Graphics Processing Unit
MC	Monte Carlo
MCX	Monte Carlo eXtreme
MM	MultiMode
MMF	MultiMode Fiber
MRI	Magnetic Resonance Imaging
NA	Numerical Aperature
NIR	Near-Inrared
NPBS	Non-Polarizing Beam Splitter
OCT	Optical Coherence Tomography
OFDR	Optical Frequenccy Domain Reflectometry
OFTD	Optical Time Domain Reflectometry
ORC	Optical Reflection Coefficient
ORI	Optical Reflection Index
PC	Polarization controller
PCF	Photonic Crystal Fiber
RC	Reflective Collimator
RMSE	Root Mean Squared Error
ROI	Region of Interest
RSH	Reflective Scanner Head
SFR	Single Fiber Reflectance
iSFR	Imaging Single Fiber Reflectance
SM	Single Mode
SMF	Single Mode Fiber
SNR	Signal to Noise Ratio
SQP	Sequential Quadratic Programming
TIC	Time Interval Counter
VCO	Voltage Controlled Oscillator
VIS	Visible

Contents

1 Introduction

Medical imaging is a cornerstone in modern medicine, providing essential non-invasive insights into the body's internal structures and physiology [1–3]. Among the various well-known technologies currently employed, such as computed tomography (CT) and magnetic resonance imaging (MRI), optical coherence tomography (OCT) has also emerged as a notable, relatively new modality. OCT is often considered the optical counterpart to ultrasound (US) imaging. Unlike US, which relies solely on the temporal measurement of back-reflected waves, OCT employs interferometry to generate high-resolution, cross-sectional images. This method achieves resolutions on the micron scale, providing remarkably detailed views of tissue structure [4]. The introduction of OCT can be traced back to 1991, with the pioneering work of Huang et al., who first brought this technique to light [5]. Over the years, OCT has undergone substantial advancements and has become increasingly popular, particularly in ophthalmology, where it is now a standard diagnostic tool [6]. Despite its widespread use in this field, the broader adoption of OCT in other medical disciplines and its recognition beyond academia remain limited. In cancer detection, for instance, OCT has demonstrated significant potential repeatedly over the past decade [7–9]. Additionally, the technology's miniaturization and compatibility with optical fibers enhance its applicability in various endoscopic applications [10]. However, OCT still faces challenges in achieving widespread clinical implementation and integration across healthcare settings. Achieving a potential breakthrough can be facilitated by integrating OCT with complementary methodologies, enabling a more complete sample examination and thereby improving diagnostic accuracy [11, 12].

While OCT can generate high-resolution cross-sectional images, it does not provide molecular contrast. This limitation makes combining OCT with biomolecular imaging techniques, such as fluorescence imaging, multiphoton microscopy, and spectroscopy, particularly interesting. Attendu et al. investigated the potential of integrating spectroscopic imaging with OCT and found promising results [13]. Spectroscopy involves analyzing the differences between the input spectrum and the spectrum retrieved after light interacts with a sample, either through transmission or reflection. This technique enables determining a tissue's optical and biological properties [14]. When successfully integrated with OCT, spectroscopy could enhance the high-resolution images provided by OCT with additional quantitative data on various optical and biological characteristics. This combination can improve the diagnostic capabilities of OCT by providing more comprehensive tissue characterization.

Combining different imaging techniques can provide improved capabilities, but this typically also increases complexity. In our case, we aim to achieve sub-pixel co-registration between OCT and spectroscopy while also considering size constraints for potential endoscopic applications. This results in the additional complexity of acquiring the spectral data in a non-contact point scanning methodology similar to conventional OCT. This non-contact scanning introduces challenges such as glare [15], which refers to reflections from the tissue surface that have not penetrated the sample and, therefore, lack useful information about the sample's composition. Currently, this glare poses a significant obstacle in quantifying data within the combined OCT-spectroscopy system, as there is no method of estimating how much glare there is present in each pixel. Addressing this issue of glare is central to the research presented in this thesis, as it is a critical factor in allowing quantitative spectral analysis.

Glare represents a notoriously complex challenge in the field of optics, primarily due to its complex underlying mechanisms and relationship with sub-micron surface roughness that defy straightforward correction [16, 17]. It is even regarded as a fundamental issue in any standard optical acquisition system and, due to its ill-defined nature, claimed to be impossible to completely remove by Gianini et al. [18]. However, the unique nature of the current benchtop system, which combines imaging spectroscopy with OCT, sets it apart from standard camera systems. The co-registered OCT depth information and the extensive amount of spectral data per image could eliminate or precisely quantify glare in the combined spectroscopic-OCT data. Unraveling these capabilities could mark a significant advancement in addressing glare and open up the door for quantitative spectral analysis in a combined OCT imaging system.

Thesis Outline

This thesis presents the research and findings of an explorative study aimed at overcoming glare in imaging spectroscopy. **Chapter 2** begins with introducing the clinical problem that drives the development of the multimodal endoscopic system, as well as explaining the fundamental operating principles of both OCT and imaging spectroscopy. **Chapter 3** explores the feasibility of adapting current spectroscopy models to our imaging setup and geometry since a model is necessary to extract quantitative information from spectral data. We hypothesize that it may be possible to incorporate glare into such a model and discuss a method

for separating glare from the useful spectral data in **Chapter 4**. This proposed method will then undergo experimental validation in **Chapter 5**. While Chapters 3, 4, and 5 focus on spectral data analysis, **Chapter 6** shifts to examining signal characteristics in the OCT data that could help in glare analysis, exploiting the fact that we have co-registered data from two modalities. Finally, **Chapter 7** introduces a technique for precisely measuring the length of optical fibers, which, although unrelated to glare, is a necessary step for the sterile calibration of endoscopes.

2 Background

2.1 Clinical problem: endoscopic esophageal cancer detection

The primary clinical focus driving the development of the combined endoscopic optical coherence tomography (OCT) and imaging spectroscopic system is the detection of esophageal cancer (EC). EC represents a significant medical challenge due to its high mortality, with a mere 20 percent 5-year survival rate [19]. One of the contributing factors to this grim statistic is the typically late diagnosis of EC, mainly originating from the absence of effective screening protocols and the asymptomatic nature of the disease. Currently, early pre-cancerous diagnosis relies on video endoscopy and biopsies, which have serious drawbacks. The changes in esophageal tissue in early stages are minimal and therefore pose a challenge for visualization using conventional endoscopy [20]. Therefore, additional random biopsies are taken for pathohistological examination. This reliance on random biopsies introduces a significant potential for errors, primarily due to the limited sampling volume, which typically represents only a small fraction of the affected area [21].

Table 1: Stage distribution and 5-year relative survival by stage at diagnosis for 2010-2016 [19].

Stage at diagnosis	Stage distribution	5-year relative survival
Localized (confined to the primary site)	22%	36.6%
Regional (spread to regional lymph nodes)	30%	20.2%
Distant (cancer has metastasized)	35%	4.1%
Unknown (unstaged)	13%	12.3%

Moreover, besides the need for earlier, more precise, and cost-effective EC diagnosis, there is a scientific reason for selecting EC detection as the primary pre-clinical application. The straightforward, tubular geometry of the esophagus makes it ideally suited for imaging with radially scanning endoscopic OCT probes. Additionally, since the esophagus is more accessible than other tubular structures, such as blood vessels or the intestines, it presents an attractive opportunity for validation purposes. Notably, ongoing efforts have already been directed toward developing and optimizing radially scanning multimodal endoscopic OCT capsules [23–25]. The latest in-house developed capsule prototype [13], is displayed in Figure 2a. Before miniaturization and clinical translation, several challenges need to be overcome, and therefore, this endoscopic capsule will not be part of this thesis, and all experiments will be conducted on a benchtop system, which is introduced in Chapter 5.

While standalone OCT has shown promise in cancer detection [7–9], it does not offer the molecular contrast or the cellular resolution critical for early cancer diagnosis. Although the detailed 3D cross-sectional images of esophageal tissue (Fig. 2de), which primarily display the layers of the esophageal wall, can detect conditions such as metaplasia and dysplasia, their accuracy may fall short of the recommended thresholds needed to replace current clinical procedures [26]. Precise identification of dysplastic tissue at the cellular
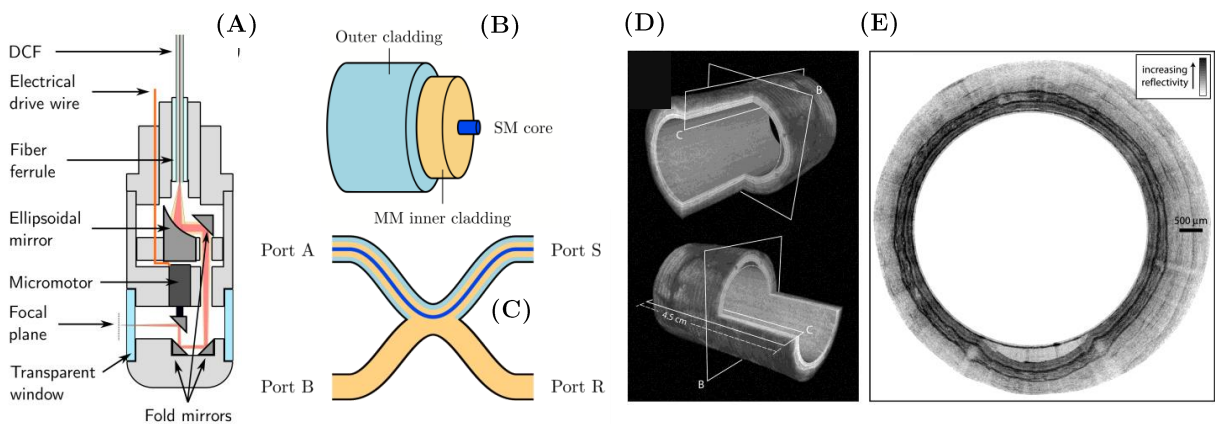
Figure 2: (A) Schematic overview of the reflective-component-based endoscopic probe developed for multimodal OCT as proposed by Attendu et al. [13]. The design strategically uses only reflective elements to minimize undesired chromatic effects. The probe has a comprehensive 360-degree scanning capability. **(B)** Illustration of a DCF. **(C)** Illustration of a DCFC. **(D - E)** Three-dimensional reconstruction of a swine's esophagus, acquired using a different OCT-integrated probe [22] to illustrate tubular 3D esophageal OCT imaging.

level is crucial in EC and early detection of various other cancers [27, 28]. Therefore, integrating OCT with a modality with greater sensitivity to these early cancer markers would significantly improve diagnostic accuracy. This integration could indicate alterations like changed nuclear-to-cytoplasmic ratios in epithelial cells, neovascularization, and differences in stromal characteristics. These variations are thought to affect tissue scattering properties and chromophore concentrations [29, 30], which are detectable through spectroscopic methods [31–37].

One of the core components enabling a multimodal endoscopic OCT system - and therefore, an exceptionally important technology throughout this thesis - is the double-clad fiber (DCF), which consists of a single-mode (SM) core and a multimode (MM) inner cladding. These two waveguides do not interfere with each other, and the injection and extraction processes can be controlled through a double-clad fiber coupler (DCFC). A representation of these fibers and DCFC can be seen in Figure 2bc. In an endoscopic system, the DCF and an electrical wire to drive a micromotor would be the sole connection to the endoscopic capsule. Consequently, DCFs have been already widely employed in multimodal endoscopic OCT systems [38–40]. Integrating OCT with imaging spectroscopy is a new development that, when accurate quantification through the co-registered spectral data is made possible, could significantly enhance the system's ability to detect EC and further advance the potential of multimodal OCT technology.

2.2 Optical Coherence Tomography

The underlying principles of optical coherence tomography (OCT) can be introduced by comparing it to ultrasound technology, but instead of using sound waves, it employs light. The light travels into the sample, and by measuring the time delay and the intensity of the back-reflected light, reconstruction of the sample is possible. However, due to the exceedingly high speed of light propagation, direct measurement between distinct reflectors is unfeasible. Consequently, the fundamental principle of OCT involves measuring the delay between reflectors interferometrically using a reference mirror [41]. This principle is utilized through an interferometer, schematically illustrated in Figure 3a. Over the past decade, various data acquisition schemes and generations of OCT systems have been developed; we use a Fourier-Domain (FD) OCT system for our purposes. The system employs a broadband laser source, divided into a reference arm and a sample arm using a beamsplitter, with both beams reflecting from the respective reference mirror and sample reflectors. As a result of a difference in optical path length between the two arms, the recombination of the beams results in constructive or destructive interference due to induced phase differences [42]. Analyzing this interference pattern as a function of wavelength allows retrieval of information regarding the sample reflector's position relative to the reference mirror.

The Fourier transform of the measured interference pattern reveals the reflected intensities at specific depths within the sample, as depicted in an A-line (Figure 3b). This A-line essentially provides a 1D depth profile of the multiple reflectors, which are generally different tissue layers or structures. To generate a complete 2D cross-sectional image, multiple A-scans are performed laterally, resulting in a B-scan (Figure 3c). Extending this approach in the other direction enables the construction of 3D images, known as C-scans (Figure 3d).
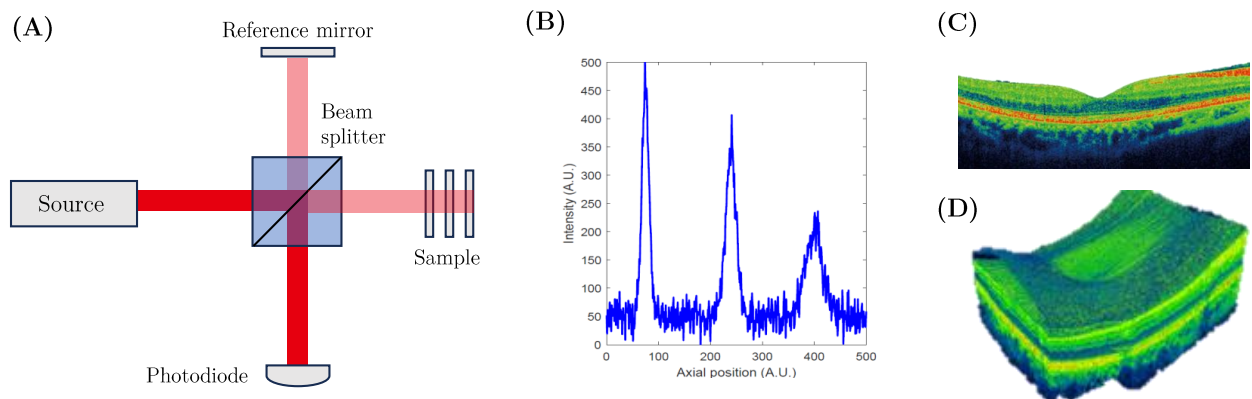
Figure 3: **(A)** Schematics of a Michelson interferometer. **(B)** Simulated example A-line of a sample with three reflectors at different depths. **(C)** Colorized B-scan of the retina. **(D)** Colorized C-scan of the retina. Both OCT example images are taken from [43].

The stated axial resolution of a few microns relates to the system's ability to distinguish between two close reflectors in the depth direction or parallel to the illumination beam. On the other hand, lateral resolution denotes the smallest distance between two close reflectors parallel to the beam's direction [44]. In OCT, these two resolutions are independent of each other: the lateral resolution depends on the focusing optics, while the axial resolution is influenced by the spectral bandwidth utilized by the laser [45]. OCT's non-invasiveness and high resolution make it extremely valuable for various medical applications. However, due to the limited penetration depth of light in tissue (0.5-2 mm), these applications mainly focus on imaging subsurface tissues, such as the retina (Figure 3cd) or skin. To extend OCT's applicability, extensive research is directed towards miniaturization for potential lab-on-a-chip [46] or endoscopic applications [26, 47, 48]. Moreover, significant efforts are being made in signal processing, enabling quantification of specific chromophores [49] or determination of blood flow velocity [50]. As mentioned in the previous section, we focus on a multimodal approach by integrating OCT with imaging spectroscopy to further enhance OCT's clinical relevance.

2.3   Imaging Single Fiber Reflectance Spectroscopy

A well-known type of spectral analysis called diffuse reflectance spectroscopy (DRS) involves two crucial components: an illuminating fiber connected to a broad-spectrum light source and a collecting fiber attached to a spectrometer (Figure 4a). This setup allows the illumination of a sample with light of various wavelengths, which then interacts with the tissue through scattering, absorption, and reflection. By analyzing the reflected spectrum of light, it is possible to extract the optical properties of the sample under investigation [51]. When there is a sufficient distance between the illuminating and collecting fibers, ensuring that the light undergoes complete diffusion within the tissue, the diffusion approximation holds, and the methods for extracting optical properties are well established. This is due to the scattering direction of diffused photons becoming randomized. Notably, the reflectance in this scenario does not depend on the exact shape of the scattering phase function $p(\theta)$—the probability distribution of scattering angles—but only on the averaged scattering anisotropy parameter g. This allows for the retrieval of essential optical properties, such as the absorption coefficient μ_a and the scattering coefficient μ_s, through the application of diffusion theory [52].

However, if the illuminating and collecting fibers are combined, known as single fiber reflectance spectroscopy (SFR) (Figure 4b), the analysis becomes only possible through empirically derived models. Since a single fiber serves as both the source and detector, the distance traveled by the photons is generally less than the transport mean free path $(1/\mu_s')$, where μ_s' is the reduced scattering coefficient $(\mu_s' = \mu_s(1-g))$. This means that most collected photons fall within the semi-ballistic regime, having undergone only a few scattering events before being collected. Modeling this using only diffusion theory fails, as one needs to account for the actual shape of the phase function $(p(\theta))$ [53]. This complicates the model needed to relate measured reflectance to optical properties, but this increased sensitivity to the exact shape of the phase function can also serve as another optical property to differentiate between tissue types [36]. Nonetheless, simulating SFR remains feasible through Monte Carlo (MC) simulations, leading to the semi-empirical model developed by Post et al., which is considered the most accurate to date [54].

In SFR, the used fiber is in direct contact with the sample, but achieving true co-registration between OCT and spectral data necessitates analyzing the same volume simultaneously, employing a point-by-point scanning approach. Consequently, the SFR fiber cannot be in direct contact with the sample; instead, light is projected onto the sample using reflective focusing optics, resulting in spectral content for each scan
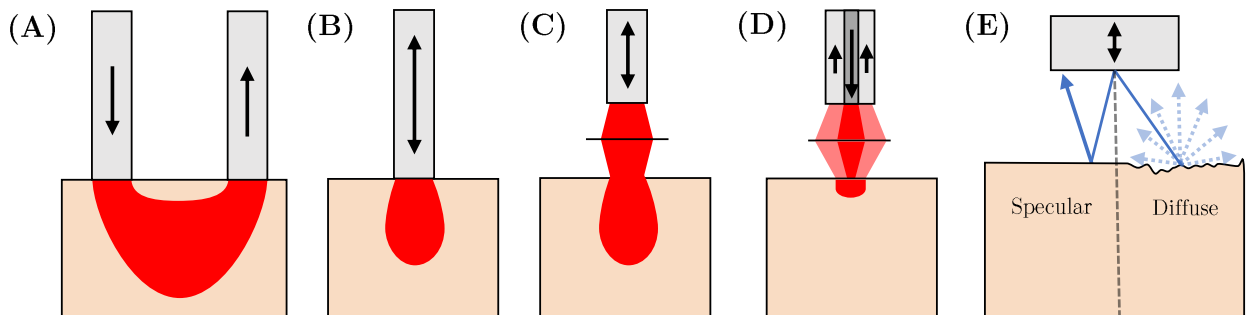

Figure 4: The different imaging geometries in reflectance spectroscopy. The dimensions are not to scale. **(A)** DRS. **(B)** SFR. **(C)** iSFR. **(D)** iSFR through DCF, in which the SM core is generally an order of magnitude smaller than MM fibers. **(E)** Schematic visualization of specular and diffuse reflections.

point obtained with a much smaller numerical aperture (NA) as in conventional SFR. This gives rise to the name: imaging single fiber reflectance spectroscopy (iSFR). Since we use double-clad fibers (DCFs) to integrate iSFR with OCT, we illuminate the sample through the core and collect the reflected light through the cladding. Different illumination and collection schemes are theoretically possible. However, light is always collected in the cladding for the current benchtop system (Section 5) since the core is used for the OCT signal. It is important to note that iSFR with DCF is again a different imaging geometry (Figure 4d). Nonetheless, in each iSFR configuration, the scanning approach results in a fine spatial resolution but also introduces a significant challenge: glare. Glare can be either specular or diffuse, depending on the tissue's texture and surface roughness [15] (Figure 4e), but in both situations, an unknown amount of light is picked up in iSFR, which is hindering quantitative analysis of optical properties.

2.4 Problem statement

Figure 5 illustrates the current capabilities of the system and highlights the problem of glare. Figure 5a presents an OCT B-scan that was co-registered with iSFR reflectance data, shown at 800 nm in Figure 5b, of a mandarin slice injected with blue dye (Figure 5c). The bright areas on the reflectance map indicate regions significantly impacted by glare. Besides some textural features, the reflectance map at 800 nm provides limited information about the composition of the mandarin.

When examining the reflectance spectra for pixels with and without the blue dye, we observe increased absorbance at non-blue wavelengths (500-700 nm). Plotting the reflectance map for normalized values at 600 nm, as depicted in Figure 5e, clearly identifies the areas where the blue dye is present. This analysis shows that, in addition to high-resolution depth information obtained from the OCT image, we can also extract data about the sample's chemical composition that is often completely unnoticeable in OCT.
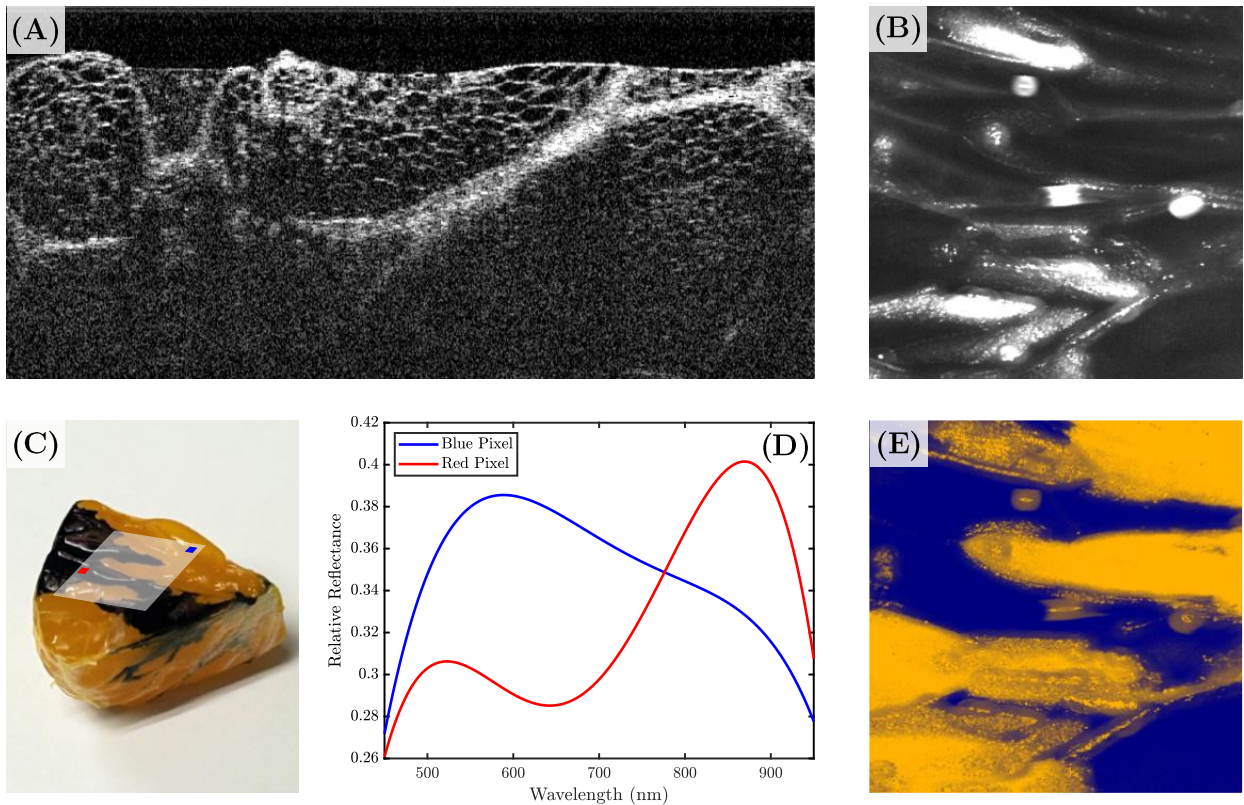
Figure 5: **(A)** OCT B-scan and **(B)** iSFR reflectance map at 800 nm of a mandarin slice injected with blue dye **(C)**. While the OCT B-scan clearly shows the sub-surface structure and layers, it fails to indicate the mandarin's altered chemical composition. **(D)** Displays the smoothed reflectance spectra from the blue and red regions, which distinctly highlight the absorption by the blue dye between 500 and 700 nm, thereby providing additional biochemical insights. **(E)** Visualization of reflectance at the primary absorbing wavelengths (600 nm) accentuates the areas infused with the blue dye. The color coding ranges from dark blue (the overall minimum) to orange (the overall maximum), mimicking the colors of the RGB image. Color reconstruction using the reflectance spectra is feasible to some extent; however, this is not utilized to create this figure.

Although distinguishing blue dye from the regular composition of a mandarin may not represent a significant scientific breakthrough, in applications such as cancer detection, the ability to assess certain biochemical properties—including blood volume, oxygenation, and bilirubin—could be diagnostically valuable. These assessments are already possible through more common forms of reflectance spectroscopy, such as DRS and SFR, as discussed in Section 2.1 and 2.3.

However, glare currently limits our ability to accurately quantify the aforementioned optical and biological properties in this novel imaging spectroscopy geometry. It is evident which pixels in Fig. 5b are severely affected by glare. Yet, in reality, each pixel may contain an unknown amount of glare. Even if minimal, this presence of glare causes offsets and distortions in the reflectance spectra (Fig. 5d), which is why we cannot currently use the absolute values from these spectra to derive accurate quantitative information.

The primary objective of this thesis is to identify a method for either eliminating or quantifying glare, thereby enabling the quantification of optical and biological properties through spectral data analysis. Physical adjustments to the laser beam, such as polarization filters, that could limit the amount of glare are ruled out since this would degrade the signal quality of the OCT. It was previously hypothesized that OCT data could be directly utilized to correct glare, given that OCT fundamentally relies on reflection analysis. However, this approach proved to be more challenging than anticipated due to differences in imaging geometry and chromatic refraction at the tip of the DCF. Consequently, we start by investigating a method to distinguish glare from useful signal using solely spectral data.

This necessitates simulating our imaging scenarios to acquire reflectance spectra for subsequent analysis (Chapter 3), developing an optimization algorithm to separate the desired spectral data from the unwanted glare (Chapter 4), and conducting experimental validation of the algorithm on samples with controlled optical properties and specular reflections (Chapter 5). This accomplishes the main objective after we present a possible methodology that can potentially identify a signal characteristic in the OCT data that could correlate with the amount of glare present in iSFR.

3 Monte Carlo Simulations

3.1 Introduction

Glare, as described in the problem statement, appears specifically within the spectral data, suggesting that spectroscopic analysis is a logical first place to start exploring ways to reduce this undesirable effect. Ultimately, one needs a model that connects the measured reflectance spectra, which may be altered by glare, with various biological or optical parameters describing the tissue or phantom being imaged. We propose that by including glare in such a model, we can separate it from the valuable spectroscopic data through a certain optimization algorithm.

Currently, no model exists that links spectroscopic data obtained through imaging single fiber reflectance spectroscopy (iSFR) to the biological and optical characteristics of the tissue being analyzed. While models exist for single fiber reflectance (SFR) spectroscopy [54–56], which collects spectral data through direct contact with the tissue (Section 2.3) it's unclear if these models are directly applicable to iSFR, given iSFR's reduced sampling volume and smaller numerical aperture (NA). This chapter will examine whether the existing SFR models can be adapted for iSFR by comparing them with forward Monte Carlo (MC) simulations mimicking an iSFR setup.

3.2 Methods

SFR Model

The SFR model developed by Post et al. is recognized as the most accurate among available SFR models [54]. It can extract several biological and optical parameters from reflectance spectra, a process that will be elaborated upon in Chapter 4. Key in the model developed by Post et al. is that the total reflectance is modeled by a diffuse part and a semi-ballistic part, where the parameter X denotes the ratio between the two:

$$R_{\text{SFR}} = R_{\text{SFR,sb}} + R_{\text{SFR,dif}} = (1 + X) \cdot R_{\text{SFR,dif}} \tag{1}$$

Photons that are considered to be fully diffused can be modeled through known analytical equations, such as the diffusion approximation to the Radiative Transfer Function (RTE) [57]. However, if we solely model SFR through diffusion theory, we do not account for the photons that only underwent a few scattering events, which we describe as being in the semi-ballistic regime. When one wants to correctly model this portion of photons as well, one needs to take into account the actual phase function ($p(\theta)$) instead of only the scatting anisotropy (g). The model by Post et al. does this essentially through the parameter X, defined as:

$$X = 3046 \left(\frac{p_{sb}}{(\mu'_s d_f)^2} \right)^{0.748} \cdot e^{-\left(\frac{1.17 \mu_a}{\mu'_s} \right)^{0.57}} \tag{2}$$

Where the coefficients were determined empirically through an extensive number of MC simulations (± 20.000) with various phase functions, tissue characteristics, NAs, and fiber sizes. A more complete derivation of the model can be found in Appendix A. The parameter p_{sb} is also derived by Post et al. and introduced in [53], which is a parameter that better describes the phase function in this semi-ballistic regime and is directly derived from the regular phase function through:

$$p_{sb} = \frac{p_b(1°)}{1 - p_f(23°)} \tag{3}$$

where $p_b(1°)$ is the probability for a scattering event in the backward direction within a 1-degree angle, calculated by the integral of the phase function over that angle:

$$p_b(1°) = 2\pi \int_{-1°}^{0} p(\theta) \sin \theta d\theta \tag{4}$$

On the other hand, $p_f(23°)$ is the probability of scattering forward within a 23-degree angle:

$$p_f(23°) = 2\pi \int_{0}^{23°} p(\theta) \sin \theta d\theta \tag{5}$$

These integration limits were determined as optimal, by analyzing the actual frequency distribution of scattering angles in SFR MC simulations and relating it to the theoretical phase function.

By comparing the outcome of this model with forward MC simulations that should represent iSFR, we could determine if the model also holds for these much smaller imaging regimes.

Simulations

MC simulations are a powerful computational technique used to model the complex interactions of light with biological tissues. By randomly sampling the paths of photons as they scatter and absorb within the tissue, these simulations provide a highly detailed understanding of light propagation and distribution in situations that can't be approximated analytically. MC simulations have become the gold standard for modeling photon transport in situations that do not adhere to, or are too complex for analytical solutions [58, 59].

We used the open-source MCX software [60] within Matlab 2023 (MCXLAB), which is a GPU-accelerated 3D light transport simulator. By correctly defining a source, detector, and medium (with spectrally varying optical properties), one can compute reflectance spectra as would have been acquired through SFR or iSFR. Throughout this thesis, the following parameters and optical properties are used for all simulations (unless denoted otherwise), with skin and soft tissue as taken an example biological tissue, according to the review of Jaques et al. [61] (Table 2).

Table 2: Used parameters to mimic skin and soft tissue in (i)SFR MC simulations.

Tissue (Skin / Soft Tissue)			Simulation		
Parameter	**Value [61]**	**Description**	**Parameter**	**Value**	**Description**
a	46.0 / 18.9	Scatter power	Volume	$6 \times 6 \times 6$ mm	Resolution 0.1 mm
b	1.42 / 1.30	Scatter slope	SFR $\varnothing_1/\varnothing_2$	300 / 600 μm	Fiber diameters
Blood %	0.01 / 0.05	Volume fraction	iSFR $\varnothing_1/\varnothing_2$	1.3 / 2.6 mm [1]	
			SFR NA	0.22	Numerical aperture
Oxygenation	0.98 / 0.98	HbO$_2$%	iSFR NA	0.05	
n	1.35 / 1.35	Refractive index	Photons	10^8	Number of photons
			λ	400 – 900 nm	Wavelength range

For every wavelength, a forward simulation is performed with the right set of optical properties from Table 2 to simulate how distinct wavelengths would have interacted with the tissue, mimicking spectroscopy. The (geometric) simulation parameters are also denoted in Table 2. All photons were launched from a point source at uniformly distributed launch angles within the specified NA. At first glance, a disk-shaped source might seem to offer a more realistic depiction. However, we strategically chose a different configuration to calculate reflectance, laying the foundation for a comprehensive simulation framework. This approach will support future large-scale Monte Carlo simulations designed to develop a model for iSFR that necessitates an extensive amount of forward simulations. Because our MC engine is based on the micro-Beer-Lamber-Law (μBLL) algorithm, which dictates that the step size of a photon is determined only by the scattering coefficient (μ_s), we can calculate the photon weights in hindsight through $e^{\mu_a \times L}$, where μ_a represents the absorption coefficient, and L denotes the photon's path length. After calculating the weight of photons, we can relate the weight to absolute reflectance as a function of radial distance ($R(r)$) by dividing it by the surface area and number of launched photons. Then we can calculate the total reflectance as a function of the desired fiber size (r) through:

$$R_{\text{tot}}(r) = \frac{\pi}{4} \cdot r^2 \cdot \int_0^r p(r)R(r)dr \tag{6}$$

with $p(r)$, being the probability density function of two points within a circle with a diameter df, given by [62]:

$$p(r, df) = \frac{16 \cdot r}{\pi \cdot df^2} \cdot \arccos\left(\frac{r}{df}\right) - \frac{16}{\pi \cdot df} \cdot \left(\frac{r}{df}\right)^2 \cdot \sqrt{1 - \left(\frac{r}{df}\right)^2} \tag{7}$$

This approach is derived from the single integral approximation in an analytical model for overlapping source and detector in diffuse reflectance spectroscopy, as presented in [57]. The approach is valid because the reflected power is only dependent on the distance between the launch and collection location (Eq. 7) and not the locations itself, which one gets when simulating a full source and detector.

---

[1]The spot size produced by projecting the fiber's surface onto a sample is inversely proportional to the ratio of the NAs. It is important to clarify that the values mentioned do not represent the DCF parameters, but rather the effective spot sizes of 300 and 600 μm fibers when the NA is adjusted from 0.22 to 0.05, representing iSFR.

One of the significant advantages of this approach is its post-simulation adjustability. By employing the entire plane as a detector and storing the complete photon trajectory, path lengths, detection positions, and exit angles, we can vary absorption properties, fiber sizes, and NAs without needing to run different forward simulations. This is because photons can simply be removed that fell outside of a specified radial distance and whose exit angle was larger than the specified NA, after which the reflectance can be calculated through Equation 6. Although storing the complete photon trajectory of every detected photon results in a vast amount of data, this method reduces the amount of forward MC simulations significantly, potentially saving weeks or even months of runtime. As employing Equation 6 to simulate SFR is a novel approach, the reflectance values for various fiber sizes, NAs and optical properties will be compared with simulations in which we specify a full disk-shaped source and detector to test its equivalence.

3.3 Results

Validation of Equation 6

Table 3 presents the calculated reflectance for a subset of fiber sizes, NAs, and optical properties, demonstrating equivalence between simulating a full disk-shaped source and detector and our proposed method based on Equation 6. The table provides insights into the results; however, actual simulations encompassed combinations of the listed phase functions and NAs (0.5, 0.22, 0.1, and 0.05), fiber diameters (200, 100, 50, and 20 microns), scattering coefficients (μ_s) of 5 and 10 cm^{-1}, and absorption coefficients (μ_a) of 0 and 5 cm^{-1}. In all simulations, the difference between the two methods did not exceed 1.8%. Experiments were repeated three times to mitigate statistical errors inherent in the stochastic nature of MC simulations.

Table 3: Reflectance comparison for $\mu_a = 5$ cm^{-1} and $\mu_s = 10$ cm^{-1}.

| Phase Function	Max NA	Size (mm)	Reflectance Full Source	Reflectance Eq. 6	% Difference
No phase function	0.500	1.000	0.050	0.050	0.650
specified, only g of 0.85	0.200	0.500	0.045	0.045	0.383
	0.100	0.200	0.036	0.036	0.183
	0.050	0.100	0.026	0.026	0.044
Modified Power of Cosines	0.500	1.000	0.131	0.130	0.963
with $\alpha = 0.8$	0.200	0.500	0.122	0.122	0.546
and order of Legendre	0.100	0.200	0.105	0.105	0.299
polynomials 0.3	0.050	0.100	0.082	0.082	0.134
Modified Henyey Greenstein	0.500	1.000	0.229	0.225	1.558
with $b = 0.2$	0.200	0.500	0.122	0.122	0.546
and $g = 0.8$	0.100	0.200	0.105	0.105	0.299
	0.050	0.100	0.082	0.082	0.134

iSFR Simulations

Figure 6 presents the results of the forward MC simulations alongside the calculations made using the existing SFR model adapted for the iSFR parameters as listed in Table 2. A difference between the simulation outcomes and the model predictions is apparent. Additionally, the attempts to fit an iSFR MC simulation with the current SFR model were unsuccessful in retrieving the correct set of optical and biological parameters.

It is important to recognize that the MC method we employed (μBLL) differs inherently from the one utilized by Post et al. in developing her SFR model (Albedo-drop). Despite suggestions in the literature that both approaches should yield identical results [63], this may not hold for cases where photons have undergone very limited scattering events. This is due to the difference in how the stepsize of photons is determined, which may result in ever so slight differences in path length distributions between the two methods and therefore affects the calculated reflectance. Consequently, we also examined whether our simulations within the conventional SFR regime would yield comparable spectra. Contrary to our expectations, the MC simulations produced spectra that deviated by an average of 5-10% from the expected outcomes, as illustrated in Figure 7.

(a) Skin   **(b)** Soft Tissue
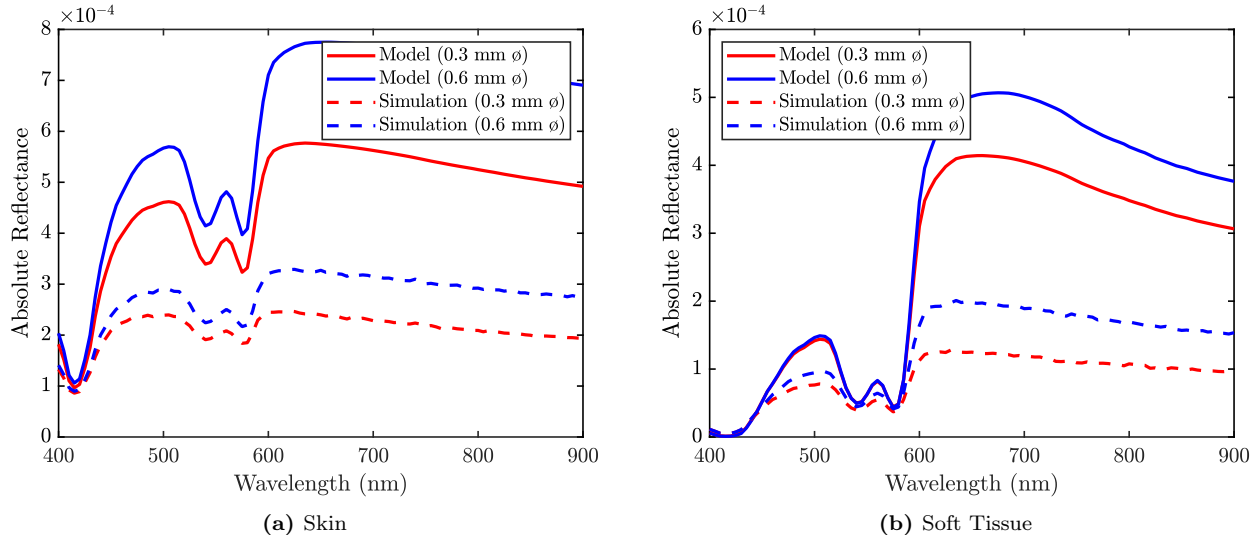
Figure 6: Resulting iSFR reflectance spectrum through MC simulations and the SFR model. iSFR parameters used from Table 2.


(a) Skin   **(b)** Soft Tissue
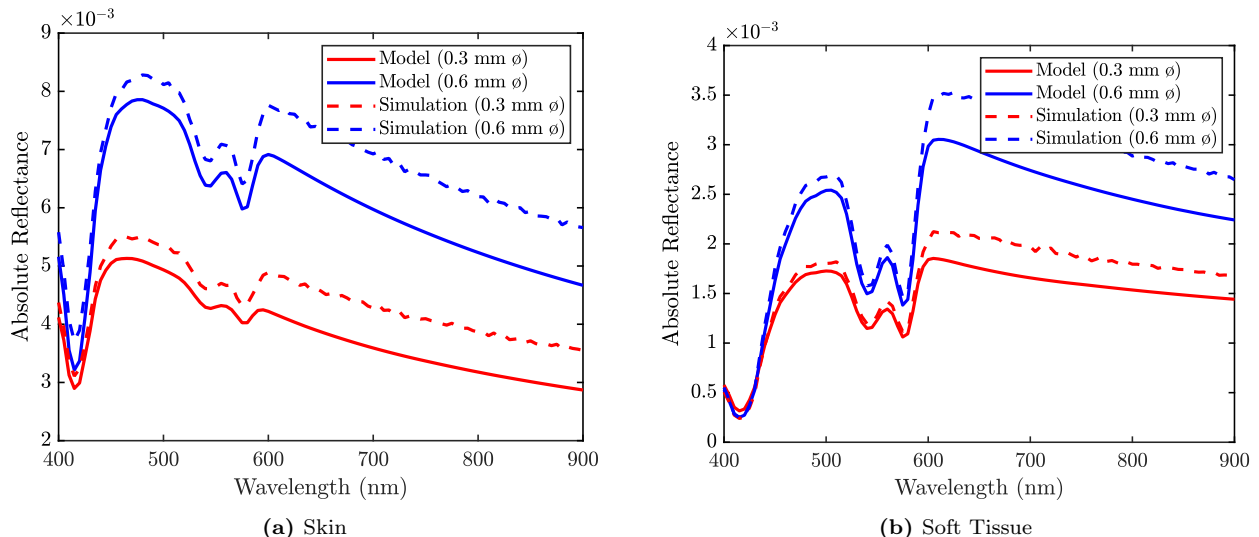
Figure 7: Resulting SFR reflectance spectrum through MC simulations and the SFR model. SFR parameters used from Table 2.

3.4 Discussion

Model discrepancies

While Figure 7 reveals differences in simulation outcomes, these deviations are notably smaller than those shown in Figure 6, which implies that the SFR model may not be appropriate for iSFR applications. This incompatibility arises from several factors. Primarily, the original model is built upon simulations that did not account for the smaller iSFR dimensions. Despite the extensive number of MC simulations performed by Post et al., their smallest simulated NA was 0.1, which is considerably greater than those in typical iSFR configurations. Moreover, the parameter p_{sb}, which is intended to characterize the phase function, might not be representative of iSFR due to the change in the quantity of scattering events and angular probabilities compared to SFR. This discrepancy is depicted in Figure 8, which shows the number of scattering events per detected photon in both modalities and also illustrates the path length distribution for all detected photons. Furthermore, the SFR model's assumption that collection efficiency can be generalized as $1.11 \times R_{\text{diffuse}}$—again, this empirical derivation—might not be applicable within the distinct non-contact iSFR geometry. Given the model's reliance on data collected at SFR dimensions and specific geometric assumptions, it is not surprising that adapting it for iSFR involves more than merely reducing the imaging dimensions.
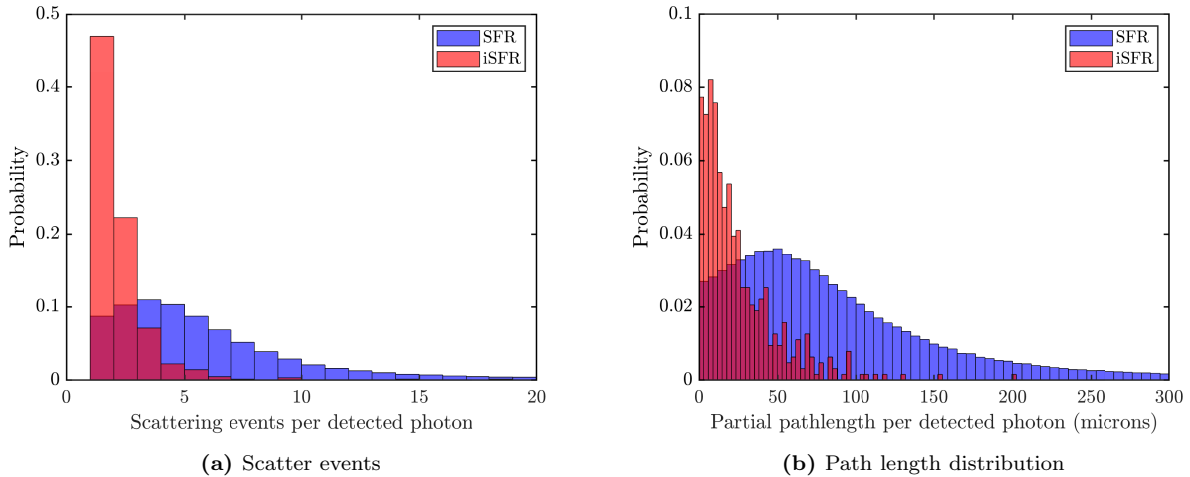
Figure 8: Differences in the number of scattering events and the path length distribution of detected photons in SFR and iSFR, as obtained through Monte Carlo simulations. The simulations were run with one hundred million photons under the following conditions: absorption coefficient (μ_a) = 1 cm^{-1}, scattering coefficient (μ_s) = 5 cm^{-1}, anisotropy factor (g) = 0.9, refractive index (n) = 1.35, diameter of SFR ($\varnothing_{\text{SFR}}$) = 300 μm, diameter of iSFR ($\varnothing_{\text{iSFR}}$) = 1340 μm, numerical aperture of SFR (NA$_{\text{SFR}}$) = 0.22, and numerical aperture of iSFR (NA$_{\text{iSFR}}$) = 0.05.

Monte Carlo differences

The discrepancies in the SFR reflectance spectra obtained from MC simulations can be attributed to two main factors. The first is the difference in the algorithms themselves. Despite suggestions in the literature that both approaches should yield identical results [63], this may not hold for the path length distributions in cases where photons have undergone very limited scattering events, due to the algorithms' step size calculation. This is a claim which should be further investigated. The second factor is the difference in simulation volume definitions. Our analysis revealed that the code used by Post et al. allowed for different refractive indices for the detector and the tissue, a flexibility our software lacks. This limitation, while it is theoretically possible to approximate with great accuracy, is not deemed significant enough to give further attention, as the next chapter will describe a possible workaround to still perform glare analysis.

3.5   Conclusion

This chapter demonstrates that existing SFR models do not seamlessly apply to the imaging geometry specific to iSFR. It underscores the necessity for developing separate models tailored to iSFR, grounded on reflectance data from considerably smaller probing volumes characterized by reduced spot sizes and NAs. Such models should accurately account for factors including collection efficiency, reflections, and semi-ballistic scattering behavior. A framework has been developed to perform MC iSFR simulations that would allow for the data generation needed for future model developments.

Furthermore, the observed results suggest the potential influence of differences in MC algorithms within these small semi-ballistic regimes. However, this could also stem from the constraints imposed by the simulation volume definition, leading to differences in SFR simulations between our work and that of Post et al. Ultimately, some assumptions stay unvalidated, which is the reason why we propose an alternative workaround, introduced in the upcoming chapter.

4 Spectral Unmixing of Glare

4.1 Introduction

Chapter 3 concluded that generating our single fiber reflectance (SFR) spectra through Monte Carlo (MC) simulations may introduce additional factors of uncertainty. On top of that, no method is currently available to relate imaging SFR (iSFR) reflectance spectra with a set of optical and biological properties. However, it remains possible to calculate reflectance spectra by utilizing the model proposed by Post et al., as detailed in Appendix A [54]. Consequently, conducting glare analysis on SFR spectra is currently the more robust option. This is because we require a model that attempts to link a spectrum with a set of properties, especially given our interest in determining whether we can accurately retrieve this precise set of optical properties in the presence of glare. Typically, an optimization algorithm is employed to fit a specific model - in our case, the one developed by Post et al. - to transition from reflectance spectrum to optical properties. This chapter explores the feasibility of modeling glare in such a manner that it can be included as an additional optimization parameter, thereby enabling the spectral separation of glare from the desired signal.

The foundational hypothesis of this investigation assumes that glare possesses a distinct spectrum, derived from the Fresnel equations, which allows for the calculation of specular reflectance for both s- and p-polarized light as follows:

$$R_s = \left| \frac{n_1(\lambda)\cos\theta_i - n_2(\lambda)\cos\theta_t}{n_1(\lambda)\cos\theta_i + n_2(\lambda)\cos\theta_t} \right|^2, \tag{8}$$

$$R_p = \left| \frac{n_1(\lambda)\cos\theta_t - n_2(\lambda)\cos\theta_i}{n_1(\lambda)\cos\theta_t + n_2(\lambda)\cos\theta_i} \right|^2, \tag{9}$$

where n_1 and n_2 represent the refractive indices as a function of wavelength of the first and second media, respectively, and θ_i and θ_t are the angles of incidence and transmission. Given that the maximal angles in iSFR are determined by the numerical aperture (NA), which is around 0.01 - 0.05, we can neglect the cosine term as this will be close to one. Moreover, since our light is unpolarized, the equation simplifies to:

$$R_{Fresnel} = C \cdot \left| \frac{n_1(\lambda) - n_2(\lambda)}{n_1(\lambda) + n_2(\lambda)} \right|^2, \tag{10}$$

with n_1 being the refractive index of air (assumed to be 1), n_2 being the refractive index of the tissue sample, and C a certain proportionality factor. Given the wavelength dependency of the refractive index, we can approximate the spectral shape of the glare.

We hypothesize that, by preliminarily understanding the spectral shape of glare, it becomes feasible to extract the set of optical and biological parameters by constructing the reflectance spectrum using an optimization algorithm. This possibility depends not only on the robustness of the selected optimization algorithm but also on the resilience of the SFR model itself. Accordingly, this chapter will evaluate the algorithm's performance in scenarios without glare and noise, with glare, and with both glare and noise, the latter scenario being most representative of real-world conditions.

4.2 Methods

As concluded in Chapter 3, the reflectance spectra obtained from our MC simulations are too distinct to be applicable within the existing SFR model. Therefore, we will rely on the SFR model itself to generate spectra. Subsequently, the developed optimization algorithm, leveraging the same underlying equations of the model, will attempt to reconstruct the initial optical and biological properties. This approach is depicted in Figure 9.

The optimization challenge is highly non-linear, and numerous methodologies exist for solving such problems, including non-linear least squares, sequential quadratic programming (SQP), interior-point methods, and genetic algorithms. However, given the vast number of simulations, speed was the most important factor in choosing our algorithm. As such, SQP emerged as the best candidate due to its superior speed, without compromising accuracy, compared to the aforementioned algorithms.

The forthcoming results are derived from analyzing reflectance spectra constructed using a set of optical parameters that simulate skin tissue, as detailed in Table 2. After calculating the reflectance spectrum, glare (following Eq. 10) and normally distributed noise were added. Given that in clinical settings, the refractive index of the sample under investigation—and its wavelength dependency—is typically unknown, the glare
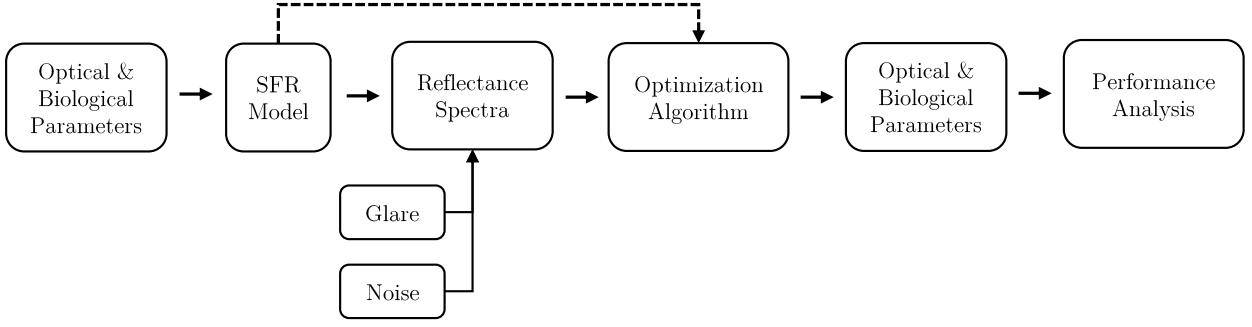
Figure 9: Workflow: We start with a set of parameters listed in Table 2, after which the SFR model (Appendix A) is used to calculate reflectance spectra. These spectra are distorted with glare and noise, after which a developed optimization algorithm tries to retrieve the right set of optical and biological properties, through the same SFR model.

spectrum was generated randomly and approximated by a second-order polynomial. This approximation involved randomly generating refractive indices at 400nm (between 1.34 and 1.37) and 900nm (between 1.31 and 1.33), and then fitting a second-degree polynomial between these points to mimic potential clinical scenarios where the refractive index spectrum can be random as well.

Post et al. hypothesized and showed that the wavelength dependency of p_{sb} could be approximated through a fourth-order polynomial, which would greatly reduce the number of fitting parameters. Centering ($\lambda_0 = 650$ nm) and scaling (10e-4 - 10e-6) results in the smallest differences between the polynomial coefficients, increasing the stability during optimization. This results in a proposed approximation for p_{sb} as follows:

$$p_{sb} = \left(p_1 \cdot \left(\frac{\lambda}{\lambda_0}\right)^3 + p_2 \cdot \left(\frac{\lambda}{\lambda_0}\right)^2 + p_3 \cdot \left(\frac{\lambda}{\lambda_0}\right) + p_4\right) \cdot 10^{-5} \quad (11)$$

The scattering coefficient (μ_s) is modeled as a power-law, centered at 650 nm through:

$$\mu_s = a * (\lambda/\lambda_0)^{\text{b}} \quad (12)$$

and the absorption coefficient (μ_a), is modeled as a weighted sum of the absorption coefficients of the individual absorbers present within the tissue, each multiplied by its respective volume concentration. For example, in a tissue composed solely of blood, the absorption coefficient is given by:

$$\mu_{a,\text{tissue}}(\lambda) = c \cdot \mu_{a,\text{blood}}(\lambda) \quad (13)$$

Here, c represents the concentration of blood in the tissue. The absorption spectrum of blood, $\mu_{a,\text{blood}}(\lambda)$, is itself modeled as a linear combination of the absorption spectra of oxyhemoglobin, $\mu_{a,\text{HbO}_2}(\lambda)$, and deoxyhemoglobin, $\mu_{a,\text{Hb}}(\lambda)$, weighted by the oxygenation level, $O_{2\text{level}}$:

$$\mu_{a,\text{blood}}(\lambda) = O_{2\text{level}} \cdot \mu_{a,\text{HbO}_2}(\lambda) + (1 - O_{2\text{level}}) \cdot \mu_{a,\text{Hb}}(\lambda) \quad (14)$$

It has been proven and shown that, to produce stable fits in SFR, one needs to acquire the reflectance spectra of two different-sized fibers. This is called multi-diameter SFR (MD-SFR) and doubles the number of data points while keeping the number of fitting parameters constant. In our case, the optimization process encompasses a total of 12 variables, as listed in Table 4. Even with glare taken into account, the number of optimization parameters (12) remains well below the number of data points (202), spanning a wavelength range of 400 to 900 nm with intervals of 5 nm.

All subsequent results adhere to specified bounds and initial conditions, deliberately set far beyond biologically reasonable values. This approach and initial guesses intentionally far from the true values demonstrate the optimization algorithm's robustness. A special non-linear constraint was set for $p1 - p4$, such that Eq. 11 could only result in values between 1e-4 and 1e-6. At each iteration, the algorithm tries to minimize the Root Mean Square Error (RMSE) between the calculated spectra via the model's equations (Appendix A) and the spectra adjusted for the current parameter values. An additional function halts the algorithm prematurely if the normalized RMSE drops below 1e-3, typically indicating an optimization parameter relative error margin between 0.1 and 0.01%.

Table 4: Optimization parameters (for skin) and descriptions.

| Parameter	Value	Initial Guess	Lower Bound	Upper Bound	Description
a	46.000	1.000	1.000	100.000	Scattering power in µs = a * $(\lambda/\lambda_0)^b$
b	1.421	1.000	1.000	3.000	Scattering slope in µs = a * $(\lambda/\lambda_0)^b$
Oxygenation	0.980	0.920	0.920	1.000	Oxygenation level tissue
Blood %	0.010	0.200	0.005	0.200	Blood volume fraction tissue
p_{sb}					Scattering statistic parameters semi-ballistic
$\quad p_1$	0.010	0.001	0.001	1.000	regime, approximated through fourth-order
$\quad p_2$	0.010	0.001	0.001	1.000	polynomial (Eq. 11)
$\quad p_3$	0.100	0.010	0.010	1.000	
$\quad p_4$	1.000	0.000	0.000	10.000	
C_1	0-1	1.000	0.000	1.000	Fresnel reflection for 1st diameter fiber
C_2	0-1	1.000	0.000	1.000	Fresnel reflection for 2nd diameter fiber
n_1	1.34-1.36	1.370	1.310	1.370	Refractive index tissue @ 400 nm
n_2	1.32-1.325	1.370	1.310	1.370	Refractive index tissue @ 900 nm

4.3   Results

The optimization algorithm

To illustrate the correctness of our optimization procedure, Figure 10 displays the performance for decreasing SNR values while the refractive indices and glare levels are known and fixed. The algorithm's performance is evaluated as the mean relative error of all fitting parameters after repeating the noise generation and optimization 30 times. This metric is shown in Figure 10 as the dashed black line where we can see that for reasonable SNR (>15 dB), the mean relative error is at most a few percent.

(a) Mean error of all fitting parameters

(b) Normalized RMSE of the spectra upon convergence
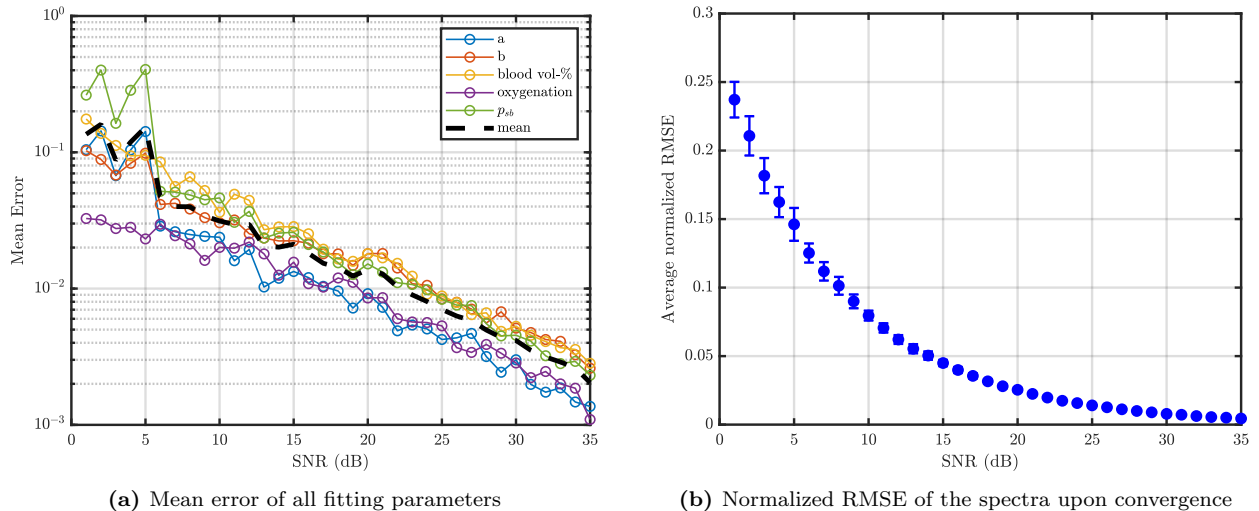
**Figure 10:** Error for decreasing levels of noise, without glare.

To demonstrate the input to the optimization algorithm and its target for approximation, Figure 11a presents an SFR spectrum measured on the skin, as specified in Table 2. This spectrum is intentionally distorted with noise (SNR of 10dB in this case) and glare (applying proportionality factors of 0.3 and 0.9 to both fibers, respectively) alongside the results after the fitting procedure (Figure 11b).

(a) Input data
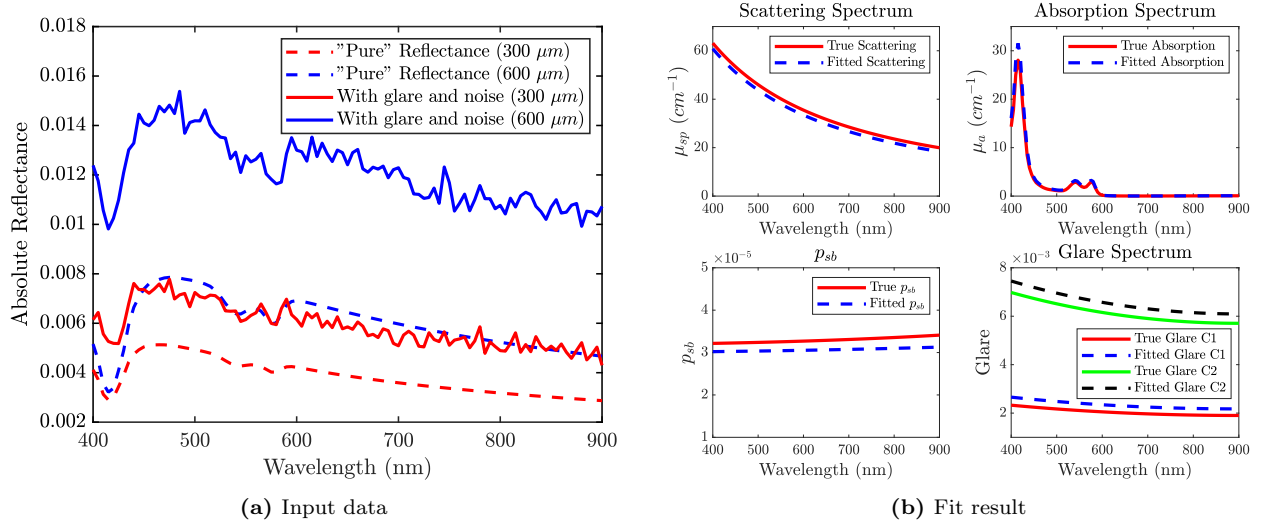
(b) Fit result

Figure 11: Example fit result where there is glare and noise added to the reflectance spectra.

Influence of glare

Figure 12 shows the mean relative error across all fitting parameters, including glare, for various glare levels in both fiber diameters, ranging from 0 (total absence of glare) to 1 (full Fresnel reflection, as described in Eq. 10). To isolate the influence of glare, noise was excluded from these simulations. The results indicate that, in the absence of noise, the optimization algorithm can extract glare and converge to accurate values for all fitting parameters, regardless of the glare level. Despite an increase in error at higher glare levels, the model consistently converges with an accuracy of less than 0.1 percent. All simulations terminated once the RMSE met the set threshold of $\leq 1 \times 10^{-3}$, suggesting that further iterations could potentially reduce the errors even more.
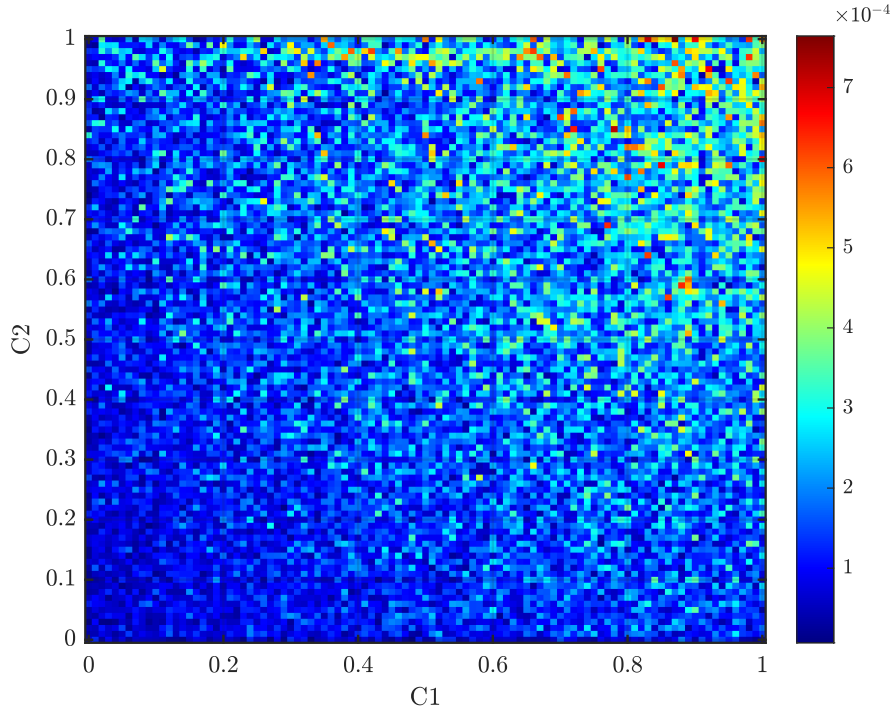
Figure 12: Mean relative error after optimization for various levels of glare, without noise.

With glare and noise

The same analysis was conducted with six levels of independent noise added to the diameters of both fibers. Ten optimizations were performed for each noise level, and the resulting errors are shown in Figure 13. Additionally, a binary map indicates which glare combinations yield a mean error that falls within a specified threshold, signifying convergence. In this context, the threshold was set at 10%. This criterion was considered acceptable for tissue classification, drawing on the findings of Post et al. in their clinical validation study on MDSFR spectroscopy [36]. Their research successfully detected differences in non-dysplastic Barrett's mucosa of patients with and without a neoplastic lesion.
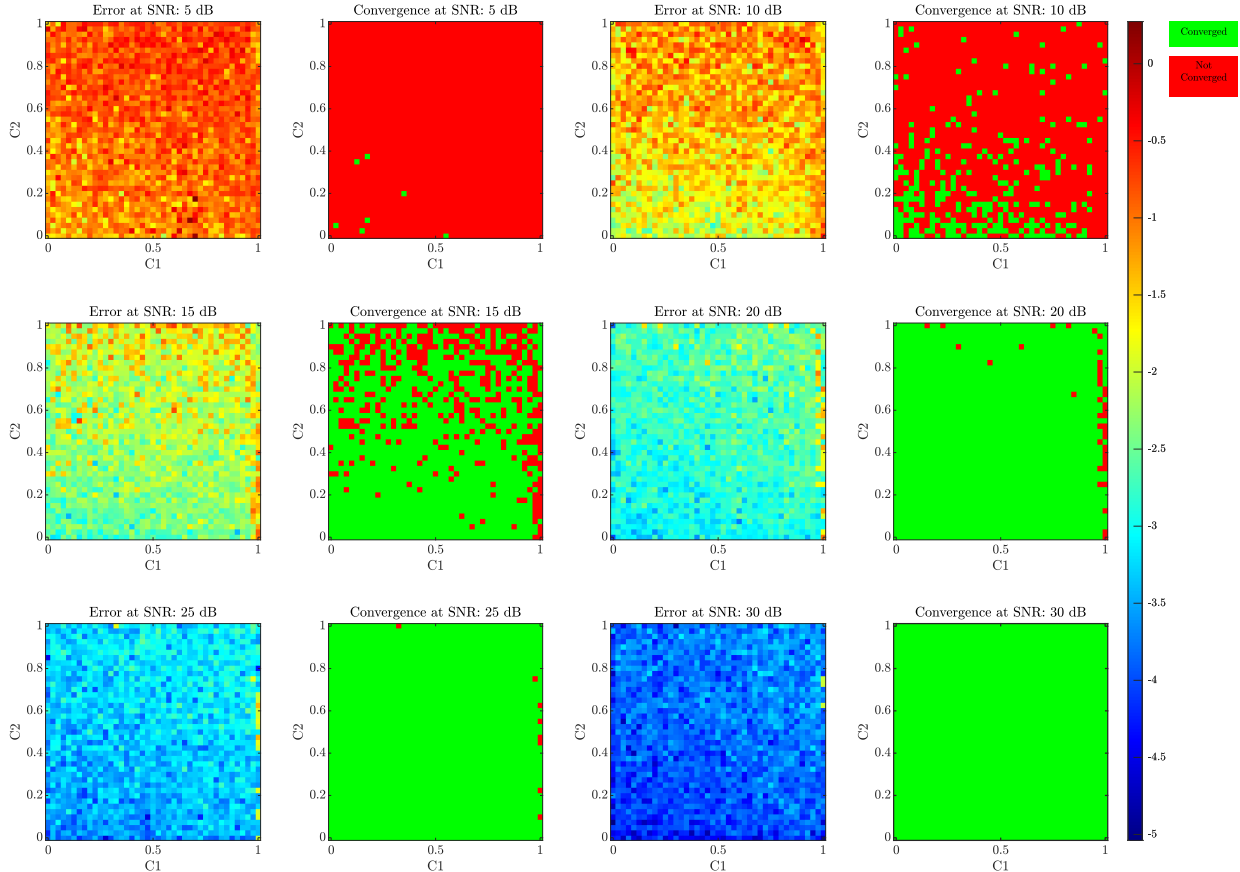
Figure 13: Convergence for various SNR and amount of glare (logarithmic scale).

iSFR levels of glare

In SFR, the absolute reflectance typically ranges from 1e-3 to 1e-4, with the Fresnel reflection being in the order of 1e-2. This suggests that spectral unmixing of the two signals is feasible, as the signal is not completely overwhelmed by glare. In contrast, in iSFR, the measured reflectance is usually around 1e-5, implying that the glare can potentially be up to a thousand times stronger than the signal itself, effectively obscuring any meaningful signal to the naked eye. Figure 14a displays the optimization performance for SFR spectra under glare up to 1000 times stronger than the signal. Physically, this proportionality factor can only be valued between 0 and 1. However, as altering our reflectance spectra to values that more closely resemble those of iSFR would prevent the model from retrieving the correct optical and biological properties, we simulate relative glare levels by scaling the Fresnel reflection by up to a thousand times. This approach mimics the relative glare to signal levels encountered in iSFR.

It was observed that by slightly narrowing the bounds and improving the initial prediction of the glare parameter—rather than allowing it to vary freely from 0 to 1000—the convergence rate improved significantly. A second error map was constructed by setting the bounds to ±350 around the actual glare value instead of ±500 (Figure 14b). This underscores the importance of having a rough initial estimate of the glare level when the glare-to-signal ratio can span several orders of magnitude.

(a) Unbounded C (b) Bounded $C(\pm\ 350)$
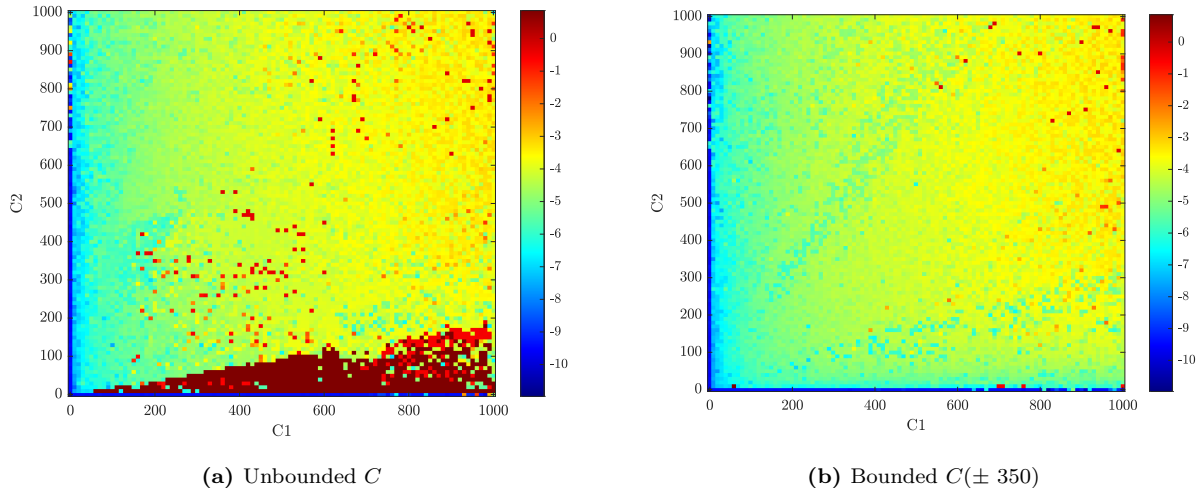
Figure 14: Error for iSFR glare-to-signal ratios.

4.4 Discussion

Clinical relevance and refractive index approximation

In most cases, we demonstrate the feasibility of effectively separating glare from the signal in SFR measurements. This separation enables the accurate determination of optical and biological parameters, suggesting the potential for integrating glare into a future iSFR model to perform quantitative iSFR analysis.

Our analysis leverages the capability to approximate the spectrum of glare using Fresnel's equation. We introduce two optimization parameters in our model, namely the refractive index at two different wavelengths. Once these parameters are fitted with a polynomial, they effectively mimic the spectral shape of the refractive index. This method, however, allows that minimizing the RMSE is feasible either by adjusting the C_1 and C_2 values or by altering the refractive indices simultaneously. This is the reason why the refractive index can not be used as an additional parameter for tissue classification.

Computational time

Achieving the RMSE convergence criterion of 1e-3 requires approximately 1 to 2 seconds per spectrum for scenarios characterized by low noise and glare. In contrast, conditions with elevated noise levels and full Fresnel reflections extend this duration to 5 - 7 seconds. Consequently, processing the biological and optical properties from an image size of 100×100 pixels-where each pixel consist of a reflectance spectrum-would necessitate roughly 12 hours without any optimizations. Although marginal improvements in the optimization algorithm itself are conceivable, they are unlikely to substantially enhance the speed of data analysis for iSFR spectra acquired under real-world conditions. The developed algorithm is well-suited for parallel computing, which means that cloud computing or GPU processing are promising options for (near)-real-time processing. Furthermore, exploring alternative approaches, such as spatial averaging methods or applying deep learning techniques, is recommended to achieve significant additional acceleration in data analysis.

Spatial averaging

To address the aforementioned points regarding computational time, as well as the competition between certain optimization parameters and glare, another promising approach would be to use more comprehensive information about the sample rather than treating every pixel (and spectrum) individually. Given that tissue properties generally do not exhibit abrupt changes in reflectance spectra, it is feasible to use an average of neighboring pixels as starting conditions, a filtering method, or to reduce competition with glare. This reduction can be achieved by hypothesizing that tissue optical and biological properties (including the refractive index) do not change as drastically spatially as glare might. By applying such methods, the refractive index could potentially serve as an additional tissue classification parameter.

Extension to iSFR

Figure 14 demonstrates that our optimization routine remains effective even when glare values are up to a thousand times stronger than the pure SFR signal itself. Given that the reflectance signal measured in iSFR is considerably lower than in SFR, these glare-to-signal ratios are within the expected range for iSFR applications. Consequently, we hypothesize that the optimization algorithm developed for SFR could also be suitable for iSFR. While an iSFR model has not yet been developed, it is anticipated that it would require a similar number and nature of fitting parameters and exhibit comparable non-linear characteristics.

Complex parameter hyperspace and algorithm choice

Table 4 shows that we set all initial parameter guesses at one of their outer bounds, which, through trial and error, was found to result in the quickest and most accurate convergence. Attempts were made to monitor the progression of these parameters, aiming to gain insights into the parameter space. However, these efforts did not yield any conclusions. The model's highly non-linear nature often led to initial guesses closer to the actual true values converging to local minima rather than the global minimum.

We also explored optimization algorithms like the Genetic Algorithm [64], intending to examine the parameter space more thoroughly to locate the global minimum. Despite these efforts, these methods did not surpass the performance of SQP with the parameter settings detailed in Table 4. Unfortunately, the underlying computational combinatorial behavior within the optimization algorithm remains poorly understood, which makes it hard to pinpoint areas in which the algorithm can be improved.

Throughout our performance analysis, we used the SQP algorithm to consistently maintain a fair comparison. However, it is acknowledged that other algorithms, such as particle swarm optimization [65] and simulated annealing [66], alongside alternative error metrics beyond RMSE — such as the Huber or Quantile loss functions — theoretically offer superior performance with noisy data. Additionally, it is shown that reflectance spectra benefit from preprocessing to refine the spectral shape before its application in optimization algorithms [67], a possibility not explored in this study.

Glare predictor for iSFR

Figure 14 highlights the necessity for a preliminary understanding of the amount of glare present. Given that deriving such knowledge is relatively straightforward—by comparing average reflectance to typical absolute iSFR reflectance intensities—there exists a possibility that other signal characteristics within the co-registered OCT signal may correlate with the glare observed in iSFR. This aspect will be further explored in Chapter 6.

4.5 Conclusion

The results from this chapter demonstrate that the method we have developed effectively extracts glare from generated SFR spectra. The ability of our algorithm to handle significantly high glare-to-signal ratios suggests it could also hold for iSFR-derived spectra. Despite some uncertainties regarding this translation, the success in approximating glare as a polynomial to retrieve optical and biological properties accurately—within clinically acceptable errors—indicates the method's reliability and potential utility. While future work is needed to validate these findings in iSFR models and improve the performance within noisy data, this study lays a promising foundation for quantitative spectral analysis in a non-contact imaging geometry.

5 Experimental Validation of Glare Removal

5.1 Introduction

The optimization algorithm developed and detailed in Chapter 4 has demonstrated its efficacy in extracting underlying optical properties from the reflectance spectrum under various glare levels, particularly in single fiber reflectance (SFR) measurements. To evaluate whether the analysis and all its assumptions apply to real-world imaging SFR (iSFR) measurements, this chapter will present its performance on data acquired from the benchtop system.

To facilitate this, it was first necessary to construct and characterize a new scanning mechanism due to the malfunction of the existing scanner head. With an understanding of our imaging geometries, we can employ forward Monte Carlo (MC) simulations to replicate our experimental setup and sample. This step is crucial, as no current model exists for iSFR, yet understanding the reflectance spectrum is needed to separate it from glare. Since a direct model linking reflectance spectra to optical properties is absent, our algorithm will be adapted to solely quantify the intensity and shape of the glare spectrum, enabling its correction.

5.2 Methods

Benchtop system

As touched upon in the background, the double-clad fiber (DCF) is one of the core components enabling the combination of iSFR with OCT. These fibers consist of a single-mode (SM) core and a multimode (MM) inner cladding. These two waveguides do not interfere with each other, and the injection and extraction processes can be controlled through a double-clad fiber coupler (DCFC). In an endoscopic setup, the DCF and an electrical wire driving the micromotor would be the only connections to the endoscopic capsule.

The setup used is depicted in Figure 15, where one can observe a conventional fiber-based FD-OCT system with a modified sample arm. A supercontinuum source is combined with the OCT light and injected into the core of the DCF through a free-space beam combiner. After recollection, the broadband spectrum of light used for iSFR is extracted through the inner cladding and directed towards a spectroscope, whereas the OCT light is propagated to the SM core and continues to interfere with the reference arm. Performing iSFR through DCFs further reduces the imaging dimensions compared to the standard fiber sizes in SFR of a few hundred microns (Chapter 3), as the core of the DCF we utilized is 9 microns in diameter. It should be noted that, due to the distinct core-cladding geometry, it is not directly comparable with conventional iSFR and probably needs a model on its own. Furthermore, we can switch between illumination through the core and cladding, which makes it possible to acquire spectra with two different fiber sizes, similar to multi-diameter SFR (MD-SFR).
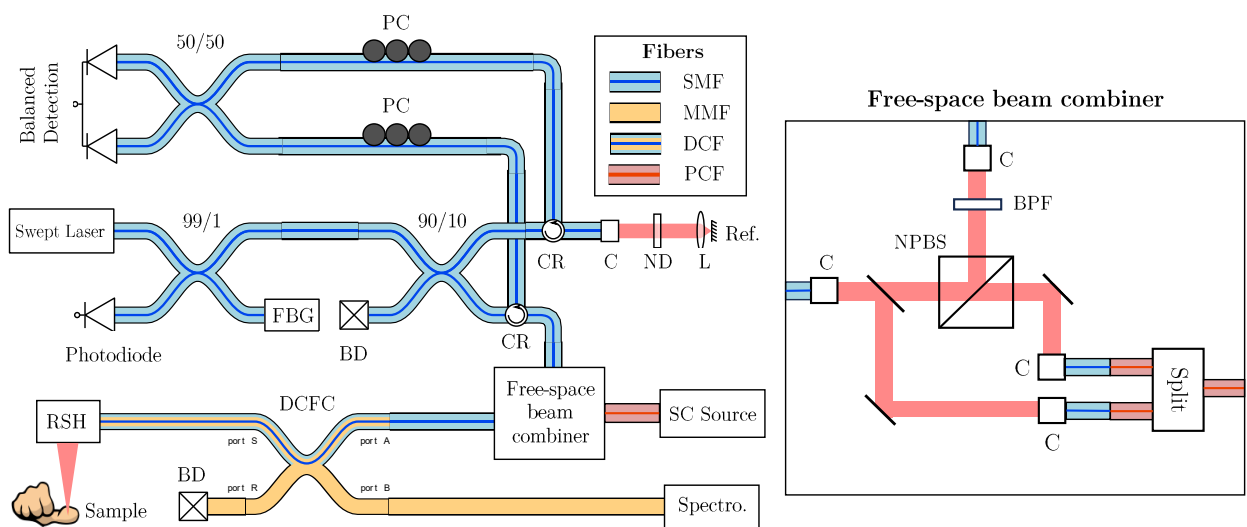

Figure 15: (PC) polarization controller, (FBG) fiber Bragg grating, (CR) broadband circulator, (C) collimator, (ND) variable neutral density filter, (BD) beam dump, (BPF) bandpass filter, (NPBS) non-polarizing beamsplitter, (RC) reflective collimator, (DCFC) double-clad fiber coupler, (RSH) reflective scanner head, (SC) supercontinuum, (SMF) single mode fiber, (MMF) multimode fiber, (PCF) photonic crystal mode fiber, (DCF) double-clad fiber.

Development of an all-reflective scanner head

Since we utilize a broadband light source for spectroscopic imaging, lenses cannot be used to focus on the sample due to chromatic aberrations and unwanted back-reflections. This is due to simple Fresnel reflections and/or the reflection of anti-reflection coatings that do not match the total spectral bandwidth. Attendu et al. demonstrated that the system is capable of imaging from 450 to 1700 nm; however, due to defects in the spectral splitter, we are limited to only using visible light (450 - 950 nm). The constructed scanning mechanism is shown in Figure 16 and consists of only reflective components. Owing to the tilt and rotation of the galvanic mirror (MR-15-30-PS, Optotune, Switzerland), several distortion effects emerge when the mirror is moved with linear voltages and the laser beam is projected onto a flat sample surface, known as the *Keystone effect*.

Two pinholes were used to align the flat mirrors (Figure 16) regarding height and direction. The parabolic mirror was fine-tuned by minimizing the spot size measured with a beam profiler (BP, BP209-VIS, Thorlabs, USA) at various axial positions. We used the beam width specified by the $1/e^2$ diameter for calculations and definitions.


(a) Schematics of developed scanner head

(b) Picture of developed scanner head
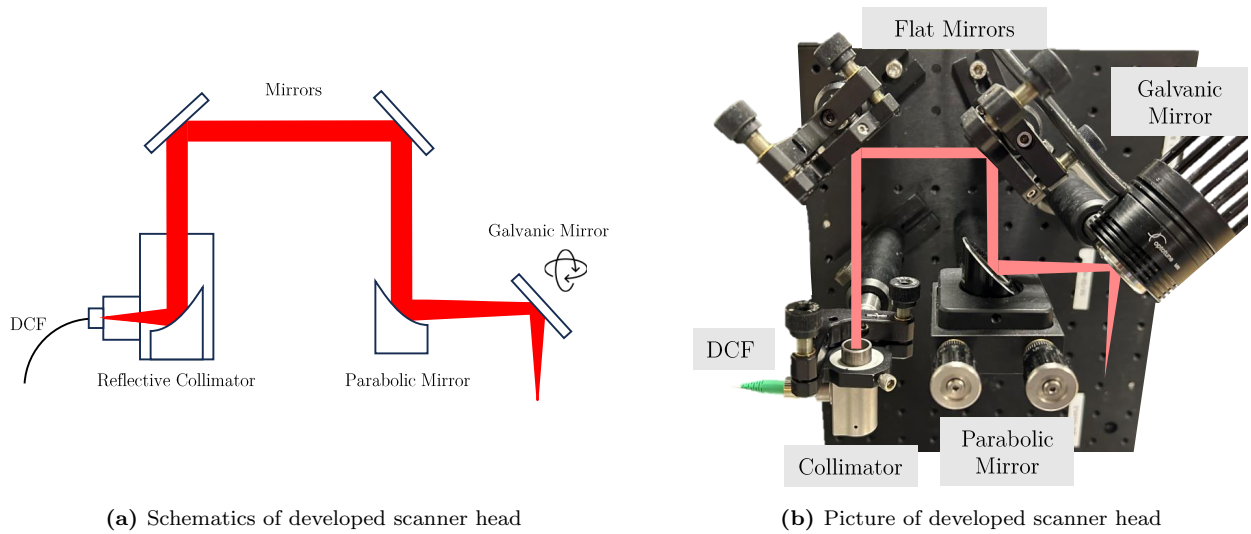
Figure 16: New reflective scanner head.

Algorithm adjustments and workflow

Given the absence of an established iSFR model, directly applying measured reflectance spectra within the developed optimization algorithm would not work. To address this, we modified the algorithm to minimize the normalized RMSE between the measured reflectance spectra for core and cladding (including varying glare levels) and a glare-free reference spectrum, presumed constant across the sample. A glare-free reference spectrum can be obtained through MC simulations or by averaging over pixels, which we know glare cannot be present due to our imaging setup. Both methods illustrate the need for a flat (liquid) homogeneous sample. Imaging a flat surface induces only specular reflections within a particular region, as is illustrated in Figure 17b.

The adjustment to the algorithm involves optimizing the refractive index at every 100 nanometers, utilizing it to calculate glare based on Fresnel equations, and subsequently adjusting by a proportionality constant. Notably, while the proportionality constants can differ between core and cladding, the refractive index remains constant. This approach builds on the hypothesis presented in the previous chapter. It is important to clarify that, due to the lack of a model for iSFR measurements, the objective here is not to quantify the sample's optical properties. Instead, our focus is on demonstrating the algorithm's capability to quantify and eliminate glare, assuming a uniformly composed sample. The total workflow, together with a schematic representation of our imaging setup indicating glare and non-glare regions, is indicated in Figure 17.

(a) Data acquisition and adjusted processing

(b) Imaging geometry
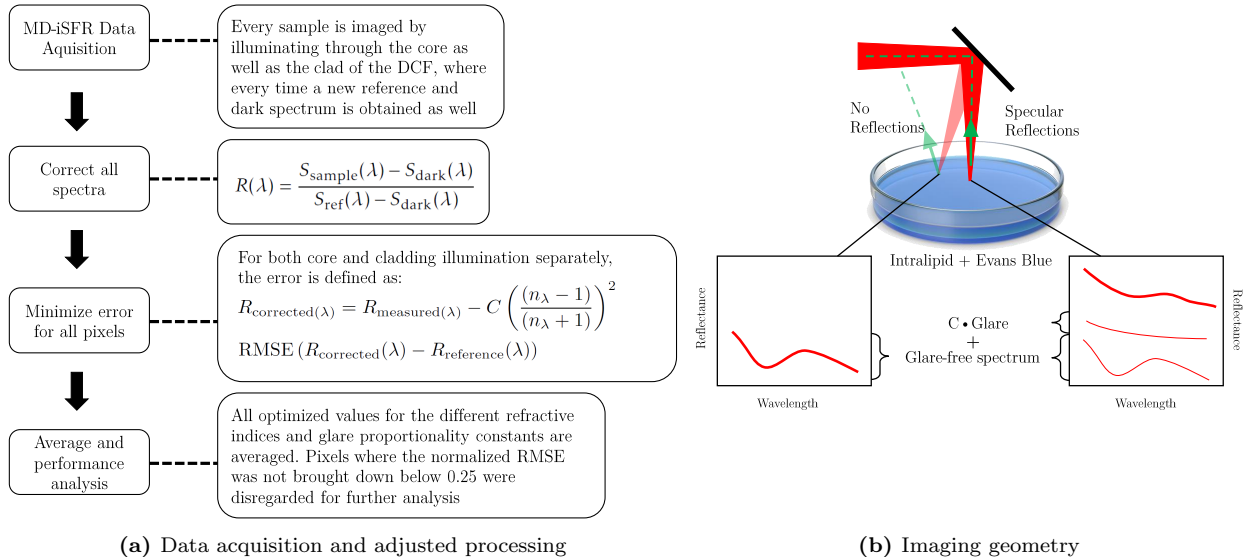
Figure 17: Schematic representation of the data processing and imaging setup.

Central to this workflow is relating the measured reflectance to the sample's reflectance by correcting for internal back reflections and the initial spectral shape of the source. Internal back reflections, not originating from the sample, should be subtracted, and the source spectrum should be adjusted by division. Back reflections are measured using a *dark* measurement, with no sample under the beam, capturing only back reflections and dark current. The source spectral shape is accounted for by using a *reference* spectrum obtained by imaging a sample, such as white paper, that should have a flat reflectance spectrum. Corrections are performed through:

$$R(\lambda) = \frac{S_{\text{sample}}(\lambda) - S_{\text{dark}}(\lambda)}{S_{\text{ref}}(\lambda) - S_{\text{dark}}(\lambda)} \tag{15}$$

Sample preparation

For our experiments, we utilized multiple Intralipid-20% dilutions (IL, RVG 02608, Fresenius Kabi, Germany) together with multiple amounts of a blue dye (Evans Blue) such that we ended up with samples that had a total scattering concentration of 20, 2, 0.5, and 0.1 vol-%. To all of these samples, Evans Blue was added in various amounts to ensure a (theoretically determined) peak absorption (at 605 nm) of 1, 5, and 10 cm^{-1}. IL dilutions were selected not only due to their low absorption but mainly because it has a (assumed) flat surface, which, upon examination of our imaging geometry, guaranteed a specific region where there were specular reflections occurring and regions where there were not, without having to deal with the complexity of diffuse reflections resulting from surface roughness. Additionally, IL's and Evans Blues' well-documented optical properties [68] are essential for generating a reference spectrum via MC simulations. This resulting spectrum, unique to both core and cladding geometries, facilitates the separation of specular reflections following Fresnel's law (Equation 10).
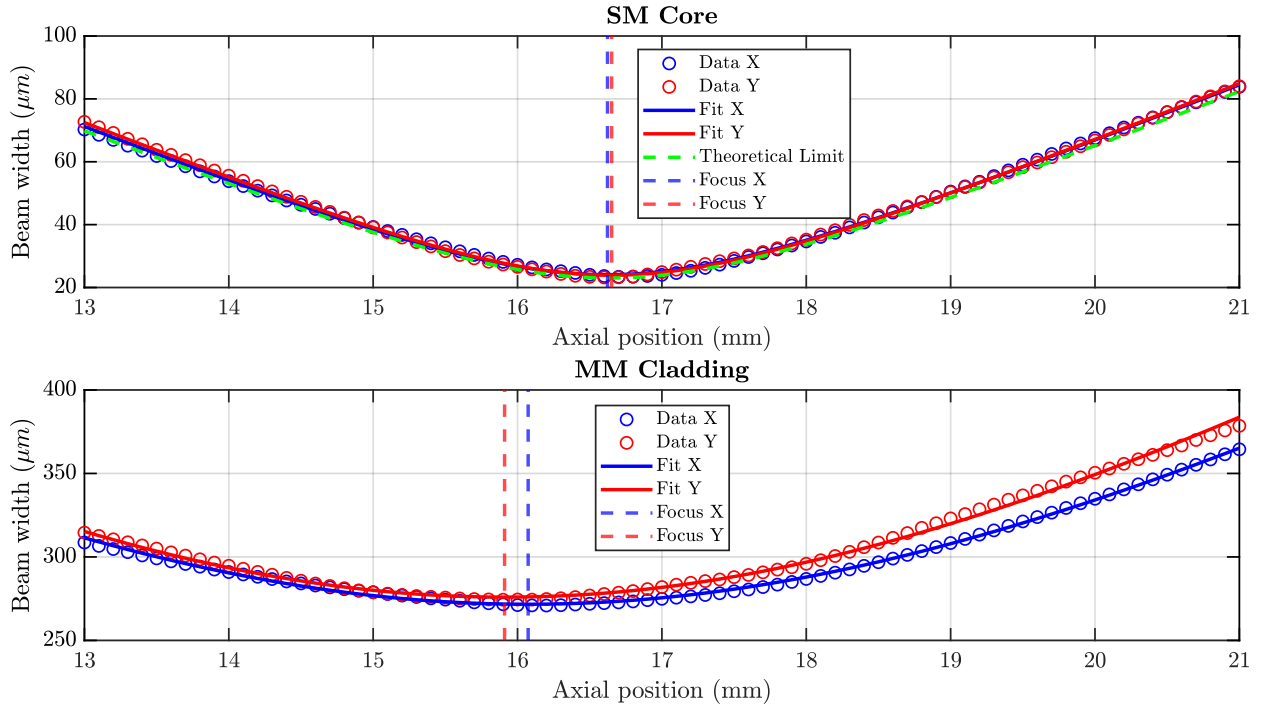
5.3 Results

Scanning mechanism

Figure 18 shows the results of the beam profiling after mirror alignment. The green line in the core configuration depicts the theoretical minimum for a Gaussian beam, indicating that we are in a diffraction-limited configuration, as one would desire. From these results, we not only directly derive the spot size and NA (needed for the MC simulation), but we can also calculate the beam width, focal point, and Rayleigh range, listed in Table 5. The minimal differences between the aforementioned parameters in the two orthogonal dimensions (X/Y (%)) indicate that there is negligible beam astigmatism. Besides profiling through axial spot size determination, the confocal point spread function (CPSF) is also determined by analyzing the maximum intensity upon mirror measurements. This reveals at what axial position our maximal light coupling back into the system occurs and gives insights into the true shift between core and cladding focus. These results are illustrated in Figure 19a.

Table 5: Comparison of core and cladding parameters

Parameter	Core				Cladding		
	X	Y	X/Y (%)	Theoretical	X	Y	X/Y (%)
Beam Width ($1/e^2$) (µm)	24.1	23.9	0.8	22.4	271.7	275.9	1.6
(Relative) Focal Point (mm)	1.662	1.665	0.2		1.607	1.591	1.0
Rayleigh Range	656	635	3.3	607	2742	2633	4.0

Figure 18: Results of the beam profiling for core and cladding illumination.
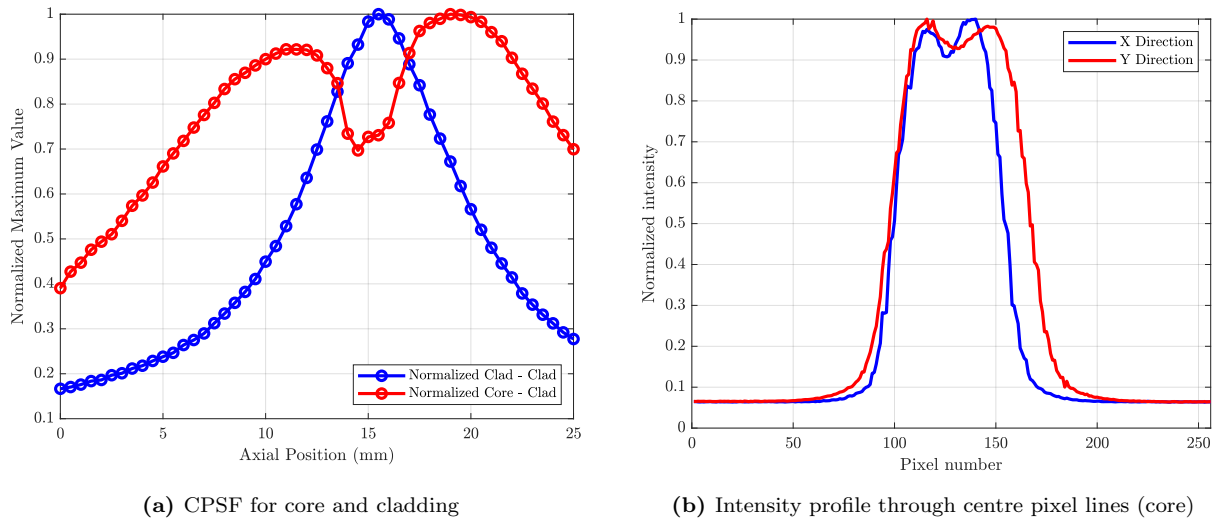
(a) CPSF for core and cladding

(b) Intensity profile through centre pixel lines (core)

Figure 19: CPSF.

The shift in the focal plane between the core and the cladding is described by the radiometric model for a DCF by Beaudette et al. [69], and as one can see from the CPSF, the actual difference in focus is negligible when considering that we can only place our sample underneath the scanner with an accuracy of ± 1 mm. This is also why we assumed the focal planes to be identical in the MC analysis, substantially simplifying the geometrical configuration. The dip in intensity around focus for the core illumination is because when

we are in focus, a large portion of the incident light is exactly back reflected onto the core again, while we only analyze the light collected by the cladding. When imaging the mirror used for the CPSF determination (which results in images like Fig. 21a), the intensity profile through the center pixels in X and Y directions shows similar behavior, as depicted in Figure 19b.

It should be theoretically possible to correct for the *keystone effect* through a series of transformation matrices to correct our linear scanning pattern to end up with equidistant sampling at the imaging plane. This turned out to be not as straightforward and rather challenging due to a combination of factors such as the angle of the incident beam, rotation of the mirror, rotation of the target plane, off-centered incoming beam, and distant center of rotation.

A more straightforward solution was to construct a non-linear geometric transformation matrix following the imaging of a calibration image, as outlined in Figure 20. This method is satisfactory for en-face image reconstruction, although it results in a non-equidistant sampling. Given that this is only an issue for bench-top geometry during wide-field imaging and not for the endoscopic probe, further attention to this matter is not deemed necessary for now.

Calibration Image with Detected Points
With Histogram Equalization and Gaussian Blur

Corrected Calibration Image
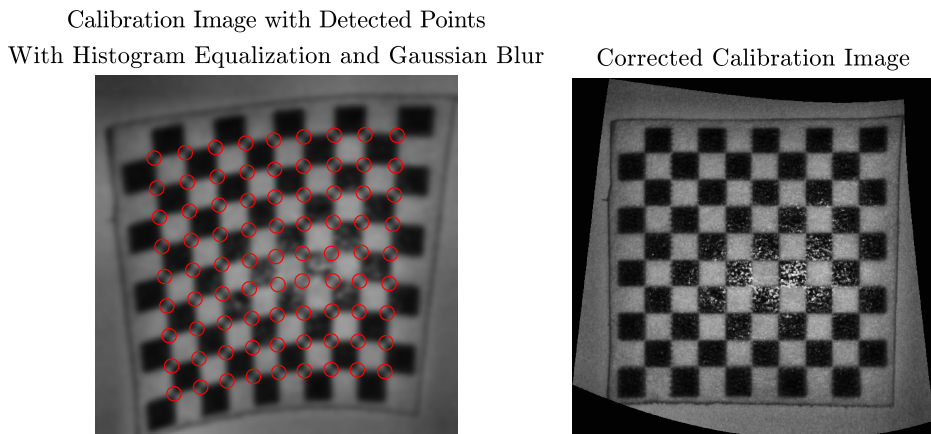
Figure 20: Calibration image of a checkerboard to perform corner detection and transformation matrix calculation.
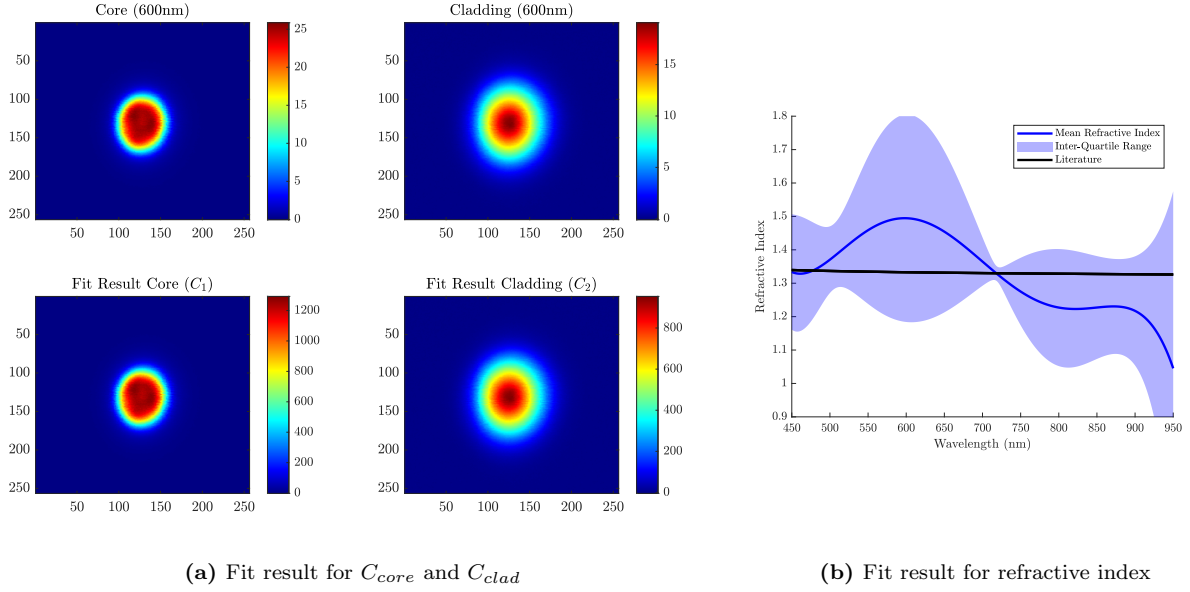
iSFR glare removal

The iSFR data at a wavelength of 600 nm, for both core and cladding illumination, is illustrated below. The bright ellipsoidal region distinctly indicates the presence of specular reflections. It is observed that the fitted values for the glare proportionality factors closely align with the original intensity image for both core and cladding geometries (Figure 21a). The decrease in intensity in the core illumination towards the center is attributed to the fact that we are collecting the reflected light through the cladding, and right at the center, a portion of the light is reflected exactly back at the core from which it is coming, resulting in a lowered intensity, also indicated through the CPSF displayed in Figure 19. Besides the glare proportionality constant, we can also evaluate the fit results for the refractive index and compare it to the known refractive index spectrum of water, given that water is the primary constituent of the samples used. This comparison is detailed in Figure 21b, highlighting that the optimization algorithm struggles to accurately retrieve the spectral shape of the refractive index as the optimized shape shows large deviations from the theoretical spectrum.

5.4 Discussion

Performance

The algorithm's failure to accurately deduce the spectral shape of the refractive index and glare stems from several factors. Firstly, there exists a direct competition between the glare proportionality factor C and the refractive index spectrum, as an increase in C can merely be offset by decreasing the entire refractive index spectrum. Additionally, the acquired spectra were of low quality, as illustrated by two pixels for both core and cladding illumination in Figure 22. Pixels not affected by glare consist of reflectance spectra as we would expect, with the absorption of Evans Blue also indicated in this example (black arrows in Figure 22b). However, the glare-affected pixels show heavily distorted reflectance spectra instead of clean and smooth summation of the glare-free spectrum and glare.

(a) Fit result for C_{core} and C_{clad} **(b)** Fit result for refractive index

**Figure 21:** Results for glare removal on the pure ILipd samples with Evans Blue ($\mu_a = 10$).

On top of that, the difference between glare-affected and non-glare pixels should mirror the spectral shape of the glare and the refractive index (Figure 22c), remaining consistent between core and cladding illuminations, assuming uniform and homogeneous optical properties of the sample. However, this was not the case for almost all pixels, particularly after correcting for dark and reference spectra, leading to inaccuracies not solely attributable to noise and potentially also the reason for the inaccurate refractive index approximation (Figure 21b). We identified a few potential sources of uncertainty that could degrade the quality of our spectra.
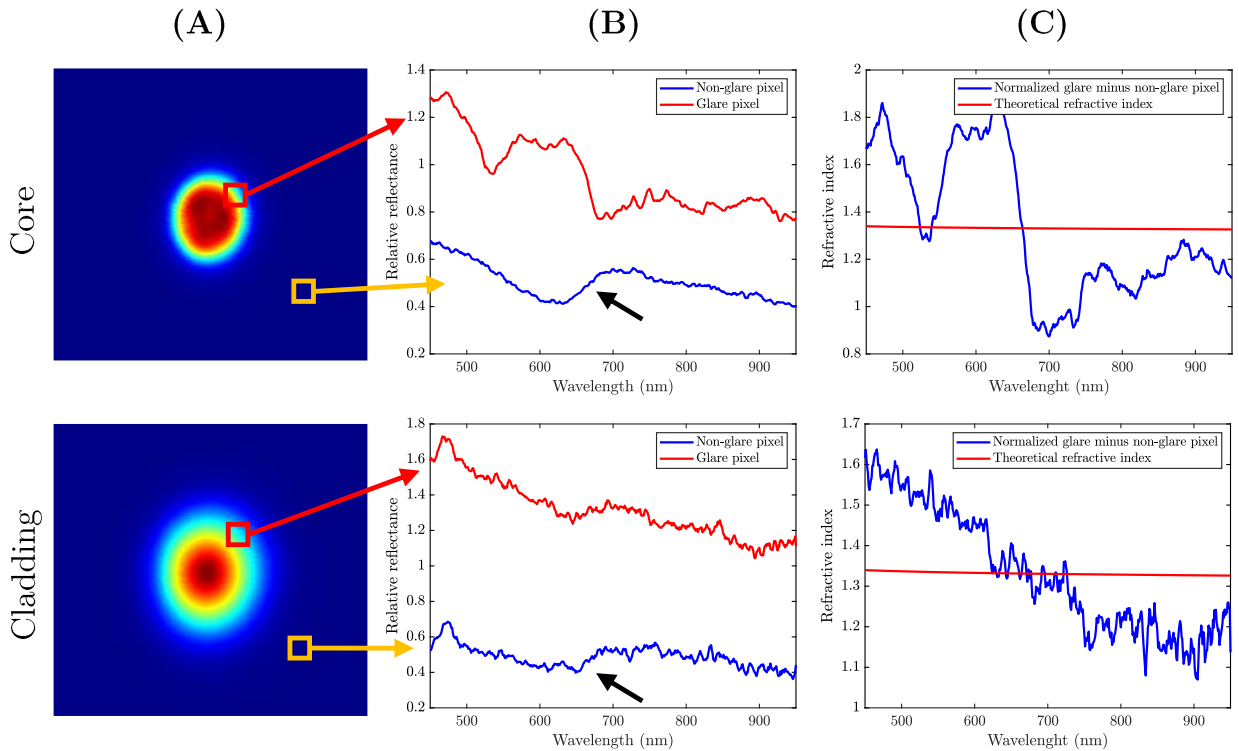
Figure 22: **(A)** Intensity image for 600 nm. **(B)** Raw example spectra for glare and non-glare pixels with the absorbance due to the Evans Blue indicated by the black arrow. **(C)** shows the spectrum's shape when we subtract the glare spectrum from the non-glare spectrum, which should match between core and cladding illumination and the refractive index of water.

Temporal power fluctuations

The temporal behavior of the supercontinuum source has been investigated previously [70] and found to have significant spectral variations as shown in Figure 24a. It should be noted that the total acquisition time of one sample can easily take up to 30 minutes, which can induce a 10% wavelength-dependent change in output power. Figure 23 shows the mean reflectance spectra, together with the standard deviation, for all spectra that make up the dark, reference and non-glare part of the sample. The change in the reference and dark spectra is minimal, as these were obtained through 100 by 100 pixels, whereas the larger sample image (256 by 256 pixels) already shows deviations that cross the reference and dark spectrum, while, for homogeneous samples, this spectrum should be constant as well. The spectra were taken from the pure IL sample with the highest concentration of Evans Blue, as it was noted that the reflection intensity from this sample was the highest while also exhibiting spectral features due to the Evans Blue. The sample reflectance was much closer to the dark spectrum for all other dilutions, resulting in a more distorted reflectance spectrum. In addition to minimizing internal back-reflections and thereby lowering the dark spectrum, we could also increase the laser output power. Although this would raise the dark spectrum, it would also enhance the sample reflectance, thereby increasing the absolute differences in counts between dark, reference, and sample spectra. However, by doing so, we saturated the spectrometer in pixels where glare was present. Since this study aimed to approximate the spectral shape and amount of glare, we had to use limited laser power and use the spectra displayed in Figure 23.

**(a)** Core illumination   **(b)** Cladding illumination
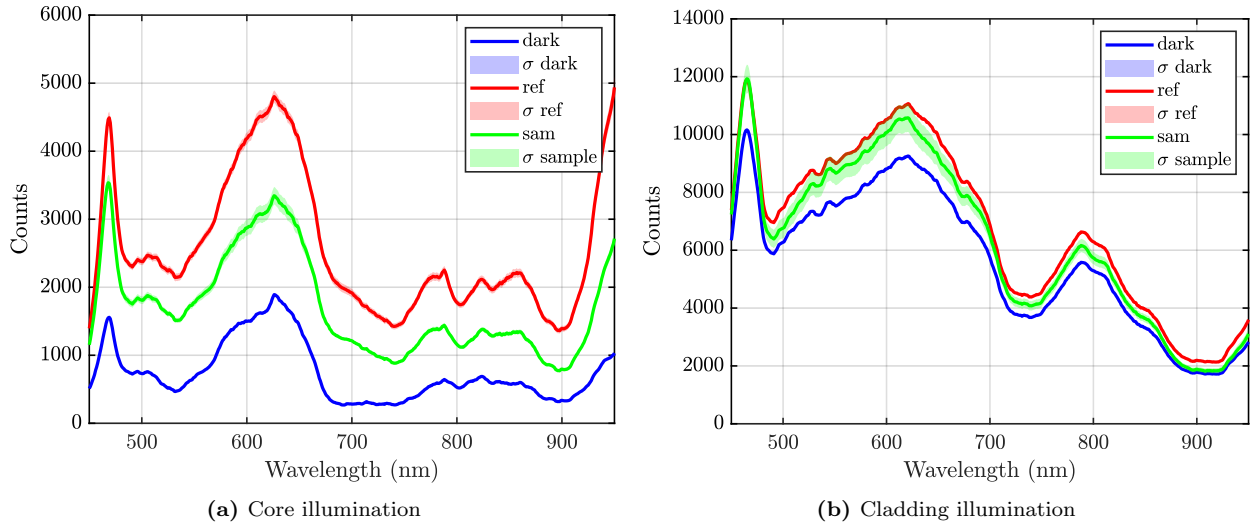
**Figure 23:** Raw reflectance spectra for the dark, reference and sample measurements.

Besides power variations during acquisition, the laser power also fluctuates between consecutive measurements as the sample has to be replaced for the reference paper, a new measurement must be started in LabView, or cables must be switched between core and cladding illumination. To illustrate this effect, Figure 25 (solid graphs) shows the average signal originating from the IL and Evans Blue (only for non-glare pixels) for both core and cladding obtained after correction with the original measured dark and reference spectrum (Figure 23). The dashed graphs show the result after the dark spectrum was altered. In this case, the counts for the dark spectrum were increased with 0 to 10% in equidistant steps over 451 to 600 nm, and wavelength 601 to 951 were adjusted from +10% to -5% to mimic power variations after obtaining the dark spectrum. Although these are entirely arbitrary values for an extreme situation, they illustrate that spectral power fluctuations between dark, reference, and sample spectra severely influence the measured reflectance, especially in situations where a limited difference exists between dark and sample spectra.

Signal intensity

Figures 23 and 25 also reveal that when the dark, reference, and sample spectra have similar intensities and even overlap, this results in a distorted reflectance spectrum, as illustrated by the cladding measurements in these figures. This partially explains the distortions in glare pixels, where, within a specific range of glare values, the sample spectrum's intensity increases to a level similar to that of the reference spectra, leading to overlaps and thus appearing as distortions in the resulting reflectance spectrum. Furthermore, a significant portion of the glare spectra is an order of magnitude greater in intensity than the dark and reference spectra. This may also contribute to distortions since certain spectral features may become more
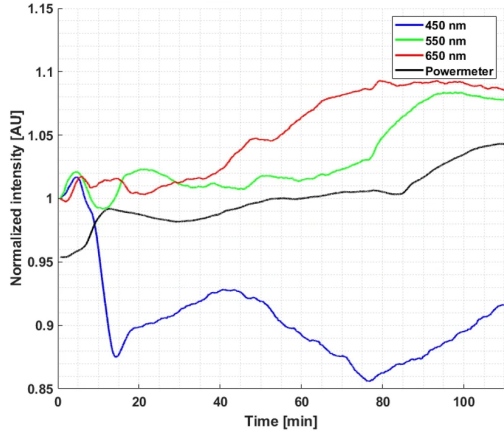
(a) Spectral fluctuations supercontinuum laser [70]
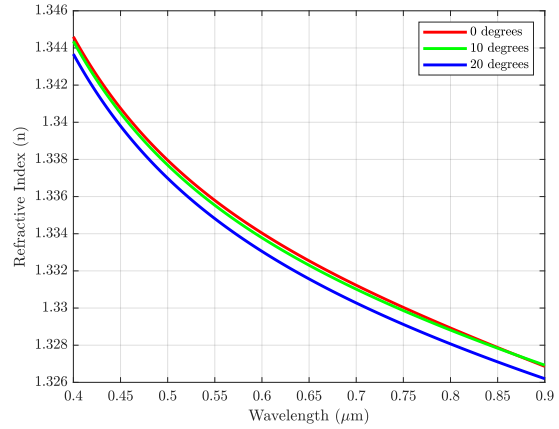
**(b)** Refractive index water

Figure 24: Possible contributors to degraded spectral quality.

pronounced and explicit at higher signal intensities. This results in apparent distortions when correcting with dark and reference spectra that do not clearly exhibit these spectral fluctuations and are an order of magnitude lower in intensity.

Temperature variations

IL samples' initial cool storing temperature and their subsequent warming due to ambient temperature and laser power exposure could introduce additional variability. Despite the minimal expected thermal impact from the laser, temperature variations are known to affect the refractive index of water, a relationship depicted in Figure 24b and calculated through the temperature and pressure relationship established by Thormähl et al. [71], though insufficient to explain the observed discrepancies.

In efforts to isolate these described factors contributing to inaccuracies, we repeated the experiments using water instead of IL, allowing the water to warm to room temperature to minimize thermal effects. Given that water has negligible scattering and absorption, it should ideally reveal no signal other than glare. This assumption sets the glare-free reference spectrum to zero and allows us to extract the dark spectrum from a region of glare-free pixels, further reducing the interval between measurements to minimize fluctuations in laser power. Unfortunately, this modification did not improve data quality, leading us to suspect that micro-vibrations or Brownian motion in the water could be influential. However, subsequent imaging with flat glass microscopy slide also failed to enhance the results.
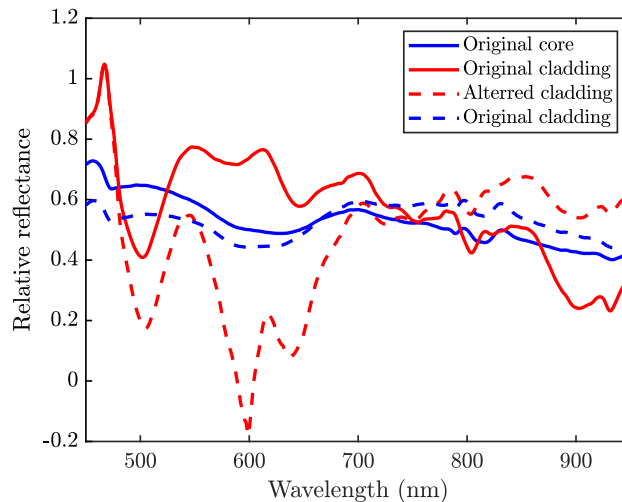
Figure 25: Illustration how a 10% variation in the dark spectrum can change the reflectance spectrum.

Furthermore, multiple data processing techniques were applied to smoothen out or approximate the acquired spectra. However, none of them could better match the refractive index spectrum to the literature, indicating that in this data, the glare-affected pixels are too heavily distorted to extract meaningful information.

Monte Carlo Simulations

The highest data quality was obtained from the pure IL samples, which led to increased signal intensities and less noise due to a higher scattering power. However, this increased scattering also introduced potential inaccuracies in our Monte Carlo (MC) simulations, as the phase function is not properly described due to dependent scattering in higher concentration samples [72, 73]. Furthermore, MC simulations yield an absolute reflectance value, necessitating either an additional calibration measurement or an estimation process to obtain accurate results. Although a fudge factor could have approximated this, the spectral shape only properly matched that of the core illumination. These remarks about the use of MC simulations need further investigation. However, for now, as we have a second method—averaging over glare-free pixels—which has fewer potential sources of error, this is the method we used in the aforementioned data processing.

MD-iSFR

This experimental validation, focusing solely on fitting the amount and spectral shape of glare, significantly reduced the number of fitting parameters compared to Chapter 4. Reflectance spectra acquired with a single spot size should suffice under this simplified model to produce stable fits compared to the previous chapters' multi-diameter approach. However, attempts to fit glare using a single spectrum did not improve the refractive index approximation. Consequently, no definitive conclusions can be drawn regarding the efficacy of switching between core and cladding illumination in our dual-clad fiber setup compared to using fibers of two different diameters.

Refractive index determination and averaging

The developed algorithm currently processes each pixel independently, and after processing the entire image, the refractive index spectrum is calculated by averaging the fit results from each pixel. However, in our experiments, we image homogeneous samples and, therefore, assume that the glare-free reflectance spectra should be consistent throughout the entire sample. This assumption suggests the potential to optimize all pixels simultaneously. Testing this hypothesis with our low-quality reflectance spectra would be inconclusive; however, this approach could serve as a method to determine the refractive index of homogeneous liquid substances. It would also reduce the competition between the amount of glare and the refractive index, as proposed in Chapter 4.

5.5 Conclusion

Unfortunately, the heavily distorted glare-affected pixels, for which we have not identified a definitive cause, prevented us from testing the optimization algorithm on the acquired iSFR spectra from our benchtop system. Determining the cause of these distortions is crucial for the future development of not only glare removal but also iSFR technology as a whole. Nevertheless, our attempts to quantify the amount of glare provided valuable insights into the optimization and acceleration of the algorithm, as well as the system improvements we have implemented along the way.

The investigation into the laser power fluctuations and signal intensities revealed that they have the highest chance of causing distorted reflectance spectra. Still, they should be investigated further as we have not yet quantified the induced uncertainties and distortions. However, we expect them to be the leading cause of poor data quality, and fortunately, both can be accounted for. Spectral power fluctuations can be monitored with wideband multimode circulators and an additional spectroscope, as proposed in [70]. The dark spectrum can be reduced by cleaning all fibers and using refractive index matching gels at connectors. Furthermore, using the full spectral bandwidth from 450 to 1700 nm would also improve the general robustness of iSFR spectra as the amount of data points will increase substantially. All in all, there is still a lot of room for improvement, both hardware-wise and in terms of data processing, that needs to be investigated further and resolved before accurate quantifications can be made.

6 Preliminary OCT Signal Analysis

6.1 Introduction

The background outlines that the fundamental principle of optical coherence tomography (OCT) involves analyzing coherent back-reflected light. This led to the initial hypothesis that there might be a linear relationship between the amount of glare present in imaging single fiber reflectance (iSFR) spectroscopy and the OCT signal intensity at the tissue surface, which would serve as the first and most prominent reflector. However, T. Koopman et al. discovered that such a linear relationship does not exist, attributing this finding to differences in the numerical aperture (NA) between the core and cladding used to collect light for OCT and iSFR, respectively [74]. Another significant issue identified was that the 1300 nm OCT light refracts at the fiber tip under a slightly different angle than most of the broadband spectroscopic light, resulting in altered projection locations for both modalities as a function of wavelength. Furthermore, when attempting to correlate the amount of glare with the ratio of signal intensity in OCT between the first layer of the sample and the intensity from the remainder of the sample, the results and conclusions were deemed inconclusive due to focusing problems and dispersion-like artifacts.

The findings from Section 4 suggest that it would be beneficial to have an indication of the amount of glare present. Building on the insights and suggestions from the research of T. Koopman et al. [74], this chapter presents a potential methodology, accompanied by some preliminary results, to further explore the relationship between OCT and glare. This relationship may be non-linear, valid only locally, or wavelength-dependent, as indicated by T. Koopman et al. Consequently, the forthcoming analysis will incorporate multiple OCT signal characteristics. Unfortunately, the time available for a thorough analysis and to address newly identified issues was very limited, as the problems with the OCT system were resolved only towards the end of the research period. Therefore, the work presented in this chapter is preliminary, and no definitive conclusions should be drawn. Additional experiments and analysis are required, as the next section will demonstrate. Although the ideas and results discussed in this chapter deserve a more detailed examination than time allows, this new set of ideas and preliminary findings could provide a solid foundation for further investigation into the potential relationship.

6.2 Methods

OCT characterization and calibration

First, the dispersion-like artifacts had to be overcome. Our initial hypothesis was that they originated from a defect or scratch in the scanner head. However, the artifacts persisted even after rebuilding the scanner head, as described in Chapter 5. We then utilized our novel Fiber Length Measurement System (FLMS), introduced in Chapter 7, to measure all optical path lengths within the benchtop system. Despite achieving better matching of optical path lengths in the reference and sample arms of the OCT system after making patch cords, the dispersion artifacts continued. Consequently, we cleaned all fiber tips and conducted a complete spectral transfer analysis of all components. This approach finally resolved the issue. No spectra showed side lobes after performing the Fourier transform, which represents the axial point-spread function. This confirmed that no component was causing dispersion exceeding what could be numerically compensated for through the algorithm presented in [75], as further evidenced by sharp test images. This indicated that the observed image artifacts were due to improper coupling between some components in the system, either from a dirty connector or an improper connection.

Unfortunately, the analysis also revealed that the near-infrared (NIR) spectral part of our iSFR system exhibited severe interference, caused by a defect in one of the mirrors in the spectral splitter. Consequently, this issue limited the analysis in this chapter to the 450-950 nm range, as this component could not be easily replaced.

Signal characteristics

Intensity relationship

The work by T. Koopman et al. on correlating the intensity of the OCT surface signal with the amount of glare present in iSFR was hindered by issues such as dispersion-like artifacts, unfocused imaging, and refraction at the fiber tip. Efforts to overcome these artifacts in previous OCT images included rebuilding the scanner head, characterizing the length of all optical fibers involved, and assessing the spectral transfer efficiency through all components. After proper setup and recalibration of the OCT system, the hypothesis regarding the existence of a relationship should be retested. Initially, the plan was to account for refraction

at the fiber tip by exclusively comparing the OCT signal at the 1300 nm wavelength and then relating this to the entire spectral bandwidth. However, characterization of the system revealed that the NIR part could no longer be utilized. As a workaround, one can independently determine the center of our image based on maximum intensities in both modalities to account for slight differences in projection location.

Given the other identified issue regarding the differences in collection geometry (also indicated by Figure 21), multiple-sized regions of interest (ROIs) can be analyzed to investigate whether more localized correlations exist. A possible local relationship might also be non-linear or more subtle within the OCT signal than the plainly processed intensity, which is why we propose investigating additional OCT signal characteristics. We briefly outline two potential candidates, which both lack a robust hypothesis but can guide or inspire the quest to find correlations in the OCT signal that may relate to glare.

Speckle

Speckle refers to a seemingly random interference pattern caused by the coherent superposition of light waves that have been scattered by rough surfaces or inhomogeneities within a medium. In biomedical photonics, this phenomenon is utilized as an imaging technique to assess, for instance, blood flow and tissue structures [76, 77]. This analysis typically involves statistical analysis of the noise-like 2D speckle interference patterns. A vast amount of literature also exists on relating speckle statistics to the surface characteristics of a sample [78], which is why we present it as a potential avenue considering that glare is also a result of surface topology [15, 16]. Speckle is also a well-studied phenomenon in OCT signal analysis [79], sometimes considered as noise [80], and sometimes found useful [81], albeit often for very different applications such as segmentation or motion analysis [82]. Moreover, standard OCT measurements can also be used for surface roughness determinations [83–85]. Despite the idea of combining the topics of OCT, speckle, and surface roughness, which has been presented previously [86], there is no literature that properly combines these three subjects and directly relates OCT speckle statistics to surface roughness. Taking it a step further and also relating the topics to glare brings along major uncertainties. It should be definitely noted that the origins and techniques in speckle surface roughness estimation generally differ from those commonly used in OCT. A second note that inherently weakens the hypothesis that such a relationship exists is that the surface roughness parameters responsible for light scattering are an order of magnitude smaller than the resolution of our OCT system [87].

General speckle statistics, such as average intensity or spot size distribution, depend on the scattering statistics of the sample but they are also significantly influenced by the characteristics of the optical imaging system's parameters, such as aperture [79, 88]. Speckle contrast and correlation are less dependent on system parameters and are widely used in material science to determine the surface roughness of a sample [89, 90]. Speckle correlation methods, however, require distinct temporal or spatial measurements, which is unfavorable in our case; therefore, we would recommend focusing on speckle contrast, skewness, and kurtosis, all solely defined through the signal's standard deviation σ and average intensity μ. Besides these standard speckle parameters, the Grey Level Co-occurrence Matrix (GLCM) of the speckle pattern is also often used for roughness estimations [91–93]. The key concept of a GLCM is to analyze how often specific intensities occur together within the image, explicitly considering neighboring pixels in specific directions.

A-line peak filtering

Another suggestion is based on the work by Saarakkala et al. [94], in which an A-Line peak filtering algorithm was applied to OCT images of cartilage to determine two novel parameters: the optical surface reflection coefficient (ORC) and the OCT roughness index (ORI), both deduced from principles already applied in ultrasound. Although the reported values of ORI are an order of magnitude greater than the optical surface roughness dimensions—consistent with the notion that the resolution of OCT systems may not be fine enough to determine roughness parameters describing scattering—the ORC might still serve as a potential glare predictor. While manipulating the A-line peak height and location may resemble the previously mentioned speckle characteristics and intensity analysis, the proposed workflow (on raw OCT data) is fundamentally different and merits thorough investigation, as the authors report significant changes in ORC values after manipulating cartilage to make it smoother.

Imaging setup

Given that the signal characteristics previously mentioned are both subtle and significantly influenced by the sample and its corresponding surface topology, a challenge is the construction of an appropriate phantom. This phantom should remain consistent throughout measurements, where the only variable is the amount of glare. This necessitates the first requirement of homogeneity, such that slight changes in position do not affect the results. Additionally, the OCT signal should originate solely from the sample's surface, as signals

from deeper regions will vary across samples and hinder the generality of any relationships identified. This implies that the scattering coefficient (μ_s) should be zero. Lastly, we must be able to control the amount of glare present without altering anything about the imaging setup or the sample itself. Identifying a particular signal characteristic that correlates with the amount of glare present in the spectroscopic data is only feasible under these conditions.

We suggest imaging a flat microscopy slide made of soda-lime glass ($n = 1.52$) submerged in water, with progressively increasing amounts of glycerol added. By varying the glycerol concentrations (from 0% to 100% weight/weight ratios in steps of 10%), we can alter the refractive index of the surrounding medium, thereby inducing changes in Fresnel reflections. Imaging at an angle allows us to eliminate reflections caused by the air-water interface. The schematics of the proposed setup and the theoretical refractive index changes of the surrounding medium are depicted in Figure 26. With such a phantom, one can be certain that all signals collected through iSFR are attributable to glare.

(a) Schematic illustration phantom setup

(b) Refractive index water and glycerol mixture
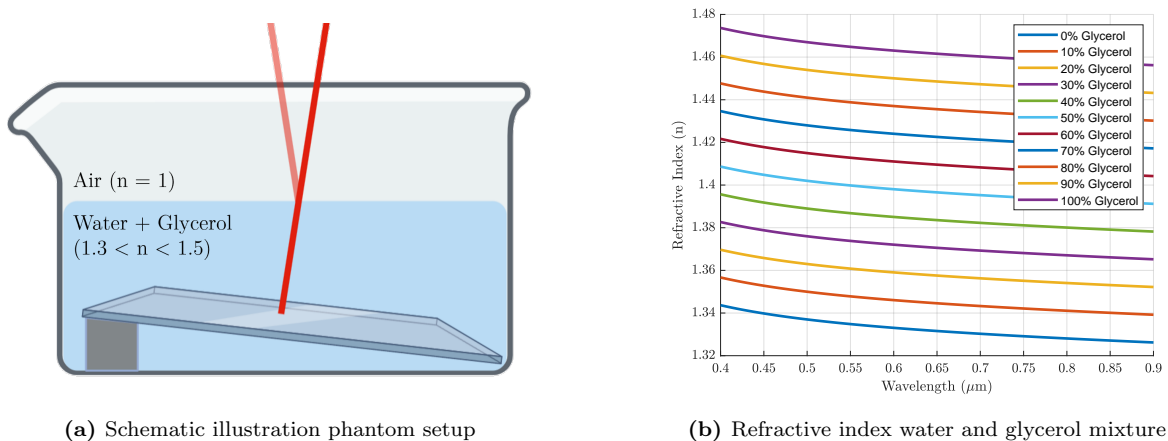
Figure 26: Imaging a flat microscopy slide with a changing refractive index should elevate the intensity of reflections, whilst changing nothing else.

Similar measurements can be repeated with sandpapered microscopy slides or comparable phantoms with known surface roughness to study the effects of diffuse reflections. This introduces another dimension to the problem, as it could help establish a relationship with surface roughness rather than glare. However, since most speckle statistics correlate more strongly with surface roughness than with reflections, this second set of measurements could provide insights into the combination of all discussed topics.

6.3 Results

An initial attempt was made to image the proposed phantom at various glycerol dilutions. Figure 27 presents the resulting images for the submerged microscopy slide with one of the glycerol mixtures. The apparent ellipsoidal shape in image 27a is attributed to the *keystone-effect*, as described in Section 5. We recommend against applying an image transformation, which would alter pixel locations and, consequently, speckle outcomes. This figure also illustrates potential ROI definitions and the pixels used to compute the dark spectrum. Figure 27b displays the accompanying cross-sectional OCT image, where the two edges of the microscopy slide are visible and the distinctino between surface signal and deep signal can be made.

We observed that for glycerol concentrations above 80%, improperly mixed bubbles and a thin additional layer around the microscopy slide appeared, which interfered with accurate intensity analysis for both modalities as the ellipsoidal shapes became heavily distorted. A preliminary intensity analysis indicated that glare decreased across all three regions of interest (ROIs) as the refractive index between the microscopy slide and the surrounding medium was better matched. This observation is illustrated in Figure 28a, alongside the theoretical Fresnel reflections at the glass-mixture interface, which roughly corresponds to the measured glare. Figure 28b also shows that the amount of signal in the OCT images originating solely from the top surface tends to decrease as the glare diminishes.

(a) iSFR

(b) OCT
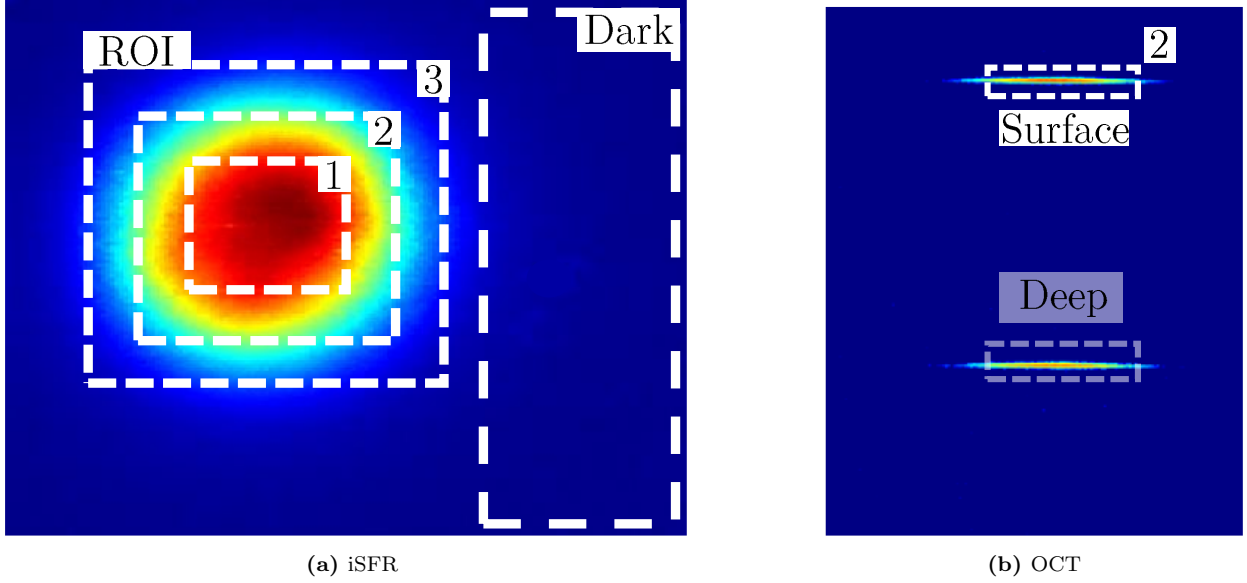
Figure 27: Imaging results of the flat microscopy slide submerged in a 20% glycerol solution. **(A)** shows the iSFR image at 600 nm, displaying specular reflections within three ROIs, as well as all the pixels used to calculate an averaged dark spectrum to correct for laser power fluctuations. **(B)** presents the OCT images, where one can clearly see the two layers of the microscopy slide.


(a) iSFR

(b) OCT
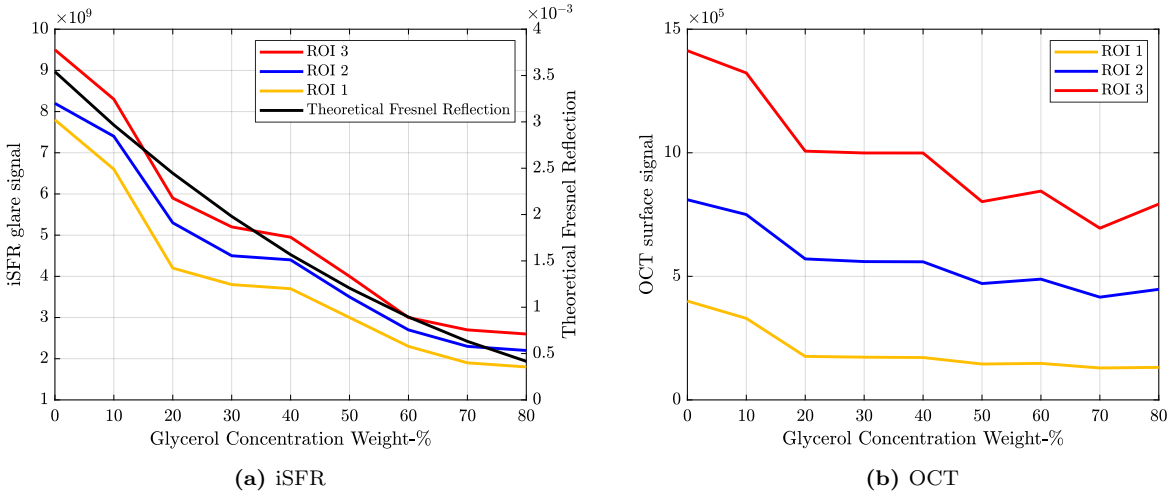
Figure 28: Signal intensities originating measured in iSFR and OCT for different dilutions of glycerol, indicating that the decrease in glare is accompanied by a decrease in OCT signal that originates from the surface layer.

Visualizing these two datasets in a scatter plot (Figure 29) reveals a potential correlation, but the limited data available prevents proper derivation of the relationship. Furthermore, it should be noted that this is merely a demonstration, suggesting that it could be worthwhile to further investigate more delicate signal characteristics, such as intensity ratios, speckles, and the ORI, which could overcome the problems identified in the previous study [74]. However, a more robust phantom and an improved measurement protocol are necessary to enhance the quality of the data.

6.4 Discussion

Relationship and significance

Figure 29 demonstrates that for three arbitrarily chosen regions of interest (ROIs), there appears to be a relationship between glare in iSFR and the OCT signal originating from the first surface. This suggests that the OCT and iSFR data might be correlated, but one has to delve into the other proposed signal characteristics, such as intensity ratios, speckle and ORC, to establish a proper relationship, as using the OCT intensity directly was ruled out due to the findings of T. Koopman et al. [74]. This preliminary
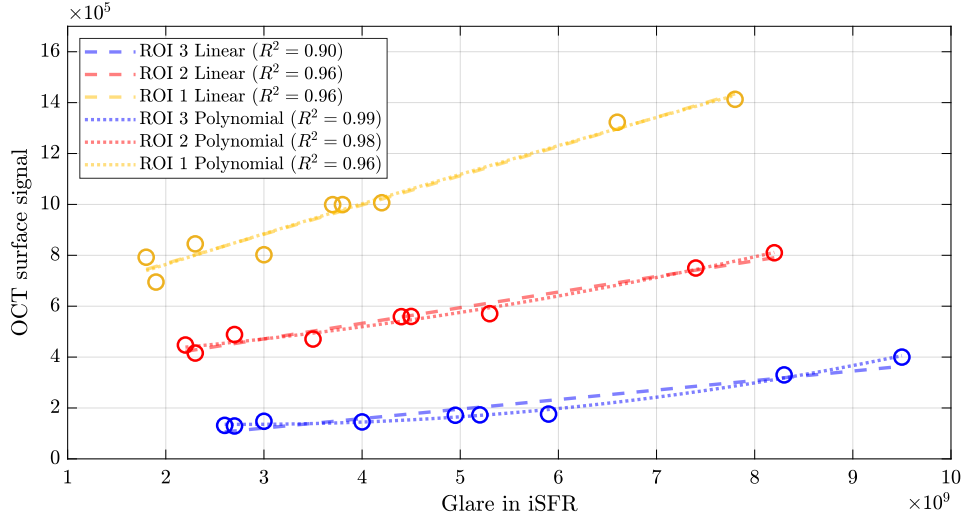
Figure 29: Correlation between glare and OCT surface signal.

data analysis also indicates that several aspects need further investigation before attempting to establish a significant relationship. This includes, for example, optimizing ROI determination and achieving better control (and sensitivity) over changes in glare to enhance the quality of the data. Additionally, it is essential to seek a physical explanation for any potentially significant relationships found. In Section 6.2, we discuss how the different subjects are connected, but a robust physical rationale supporting the hypothesis is lacking. For instance, it is plausible that any correlations found between speckle statistics actually correlate with the geometric shape of the glare pattern or surface roughness rather than the actual amount of glare.

Phantom problems

During this initial set of measurements, we encountered multiple issues with our phantom. The beaker had to be removed, the medium replaced, and then repositioned under the scanner head using several drawn markers between measurements. Although the microscopy slide was fixed within the beaker, slight displacements between consecutive measurements altered the imaging position on the slide. Consequently, it was not guaranteed that the first layer of the slide was perfectly in focus each time, which changed the back-reflected intensity. This had a significant impact, as we already lost most of our light upon the first specular reflection.

Furthermore, during the measurements, we observed a slight shift in the pixel with maximum intensity. This led to the realization that the different glycerol mixtures refracted light variably, affecting where the beam struck the slide and, more importantly, the angle of incidence. This effect, not anticipated beforehand, significantly complicates the glare analysis. Despite our efforts to construct a phantom where only the amount of glare varied, this variability needs to be accounted for in future measurements.

Generality

As we encountered challenges and realized that many considerations must be addressed to establish a clear relationship between the OCT signal and glare in iSFR within a controlled lab environment using a phantom not highly representative of tissue, this naturally tempered our expectations that such a relationship could be straightforwardly established for endoscopic imaging of various tissues. When imaging tissue, one must consider additional factors such as light from various depths within the sample, surface roughness, diffuse reflections, and non-homogeneities, all of which are likely to influence the signal characteristics we propose to study.

From the work of T. Koopman et al., it was already known that establishing a relationship was challenging due to the many considerations when comparing two completely different modalities. Nevertheless, since this benchtop system is, to the best of our knowledge, the only setup that combines OCT with imaging spectroscopy, it may be worthwhile to further explore the potential relationship. Discovering discrepancies or similarities at this stage is crucial for optimizing the future integration of this system endoscopically.

6.5 Conclusion

Despite incorporating lessons from the previous study by employing a new phantom, analyzing multiple regions of interest (ROIs), accounting for refraction at the fiber tip, and proposing a broader range of signal characteristics and non-linear relationships, the initial preliminary measurements reveal that establishing a relationship between OCT and glare is even more challenging than initially anticipated. This difficulty arises not only from the inherent differences between the two imaging modalities we are comparing but also from the need for a robust and sensitive phantom to establish and test potential relationships.

7 Fiber Length Measurement System

The primary objective of this thesis is to address the issue of glare in the current benchtop system, aiming to advance its integration into an endoscopic capsule and facilitate quantitative detection of esophageal cancer. At the onset of my research, the OCT images exhibited dispersion-like artifacts. This led to the hypothesis that an excessive mismatch in the amount of glass (optical fiber) between the sample and reference arms was beyond what the dispersion-compensation algorithm could correct. Subsequent investigations revealed that this was not the cause. However, this hypothesis initiated a deeper exploration into accurately and precisely measuring the length of optical fibers without resorting to laying the fiber out and measuring it with a tape measure. Such a need arises in complex benchtop fiber-based systems or the calibration of endoscopes requiring sterility. It became apparent that limited solutions were available, uncovering a modest research gap. Consequently, it was determined that this challenge warranted further investigation and possibly publication.

On the next page is a preliminary version of the letter we intend to refine and submit for the first round of reviews. Although the letter describes a method of accomplishing sub-millimeter standard deviation, we are still left with two main discussion points, namely the temperature dependency and the observed non-linearity. We intend to perform experiments in the near future to explain these two effects and, more importantly, to correct them, which should drive down the precision (and costs) even further.

Temperature dependency

Figure 3 in the letter depicts a very strong correlation between the measured lengths and temperature, as we conduct measurements overnight, with even the moments when the air-conditioning in the lab turns on and off also being clearly visible. The thermal expansion and change in the refractive index of the fibers account for only $\pm$ 10% of the length variations for the registered temperature changes. The 200-meter reference spool is wrapped around a plastic holder, and for a wide range of thermal expansion coefficients of plastic, expansion of the spool can induce a full centimeter per degree shift. This led to an experiment in which we completely unwound the reference fiber, but time permitted only one test measurement, and this resulted in worse instead of improved standard deviation.

Finding the cause and correcting for this temperature dependency would greatly enhance the capabilities of the proposed method. The four-hour period in which we obtain a standard deviation of only 60 microns is quite remarkable, considering the simplicity and cost-effectiveness of our setup. Achieving this standard deviation regardless of temperature fluctuations would also open the door to other applications where precise control of phase measurements is crucial, such as phase-modulated depth-resolved spectroscopy. Performing measurements in a temperature-controlled environment is also an option, but this compromises the robustness of the device, as we envision a mobile device capable of measuring parts of optical setups in various labs.

Another possibility would be to add another reference fiber, the length of which is determined with high accuracy, for example, through optical frequency domain reflectometry (OFDR). By also measuring this second reference fiber, we obtain a value (depended on the current temperature) that we can compare to the expected value, which we can then use to correct the fiber under test directly. This idea has not been tested but could potentially serve as a backup if we fail to determine the cause of the temperature variations. Performing an empirical correction through this method, instead of the linear regression method stated in Section 3.2 of the letter, requires only two consecutive measurements instead of hundreds.

Non-linearity

As we investigated the optimal frequency range for our measurements, we observed that the measured time delay depends on the length of the chosen frequency interval in a consistent manner, suggesting that the relationship between phase and frequency is slightly non-linear. We hypothesize that this non-linearity results from a certain frequency response in the system that subtly affects the phase and, consequently, our measured length. Isolating the component responsible for these induced non-linearities is a challenging task considering the minimal phase change we are dealing with, which is why efforts to overcome this issue have not yet been made. Reducing the frequency sweep to an even smaller interval could further decrease the cost of most of the required components.

Benchmarking

When the aforementioned problems are addressed, we intend to benchmark our setup with an OFDR to determine its accuracy properly.

Optical Fiber Length Measurement Method

R. van Zutphen

University of Twente / Amsterdam UMC

X. Attendu

Polytechnique Montréal / Amsterdam UMC

Abstract

Precise measurements of the length of optical fibers are increasingly needed across various applications. Many commercially available devices are either too inaccurate or, conversely, too advanced and costly for mere length determinations. We present a simple and relatively inexpensive method to measure the length of optical fibers with a precision of 0.9 mm. This method exploits the relationship between the phase difference of a fiber of interest and a reference fiber as a function of frequency. We also highlight considerations important for converting measurements from the temporal to the spatial domain.

Keywords: Optical Fibers, Transfer Delay, Length Measurements, Phase.

1. Introduction

In recent years, optical fibers have become the cornerstone of numerous critical applications, spanning from advanced communication systems [1, 2] to cutting-edge biomedical technologies [3]. The demand for more accurate and precise measurements and transfer capabilities through optical fibers has increased, leading to the challenge of precisely determining the exact optical length or optical transfer delay (OTD) of these fibers. This challenge is particularly pronounced in scenarios where, despite the impracticality of manual measurements, accurate calibration of optical components is crucial. Such scenarios could include for example intricate experimental interferometric setups [4] and medical environments that employ sterile fiber-based endoscopes [5].

Traditionally, OFTD measurements have primarily relied on time domain technologies, notably based around the optical time domain reflectometer (OTDR) [6] and time interval counter (TIC) [7]. While these methods have a remarkable range up to 100 km, they have their limitations such as low measurement accuracy (about 1 meter) and the existence of dead zones. Although these limitations are less critical for large network testing, where OTDR is predominantly used, it is ineffective for the previously mentioned applications requiring more precise measurements in the range of a few meters. On the contrary, optical frequency domain reflectometers (OFDR) [8], offer accuracy of a few microns and have a measurement range of a few 100 meters. Nevertheless, commercially OFDR systems, while advanced, come with a high cost and complex functionalities that often exceed the necessities of basic fiber length measurement.

Recently, novel systems have been introduced that exploit the phase shift experienced by the propagating light as the modulation frequency of its laser source varies [9–11]. These methods have a high dynamic range, micron-level resolution, and robust stability. However, their operation in the gigahertz (GHz) spectrum necessitates microwave modulation and phase detection, inherently increasing the complexity and costs of both the components and the overall setup.

In this letter, we introduce a method similar to these advances, yet distinguished by a less complex setup operating in the megahertz (MHz) regime. This shift allows for the utilization of a broader spectrum of lasers, modulators, and phasemeters. Moreover, we convert time delay measurements into fiber length, highlighting the potential inaccuracies and considerations essential to this process. Our approach, which simplifies both the setup and data processing, aims to introduce an innovative and more accessible method for fiber length measurements.

2. Methods

2.1. Principle

The rather simple, yet effective, principle driving this method of measuring time delays is that light, when modulated with frequency f, will experience a phase shift ($\Delta\phi$) as it traverses two unequal optical paths, given by

$$\Delta\phi = 2\pi f \Delta t \tag{1}$$

where Δt is the time difference between two paths. By measuring the phase shift between two unequal optical
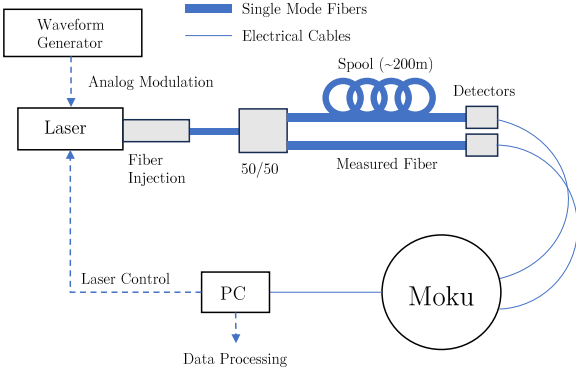
Figure 1: Schematic overview of the system

paths over a wide range of frequencies, one can obtain an accurate measurement of the time difference (Δt) between the two paths as we differentiate the linear relationship with respect to f:

$$\frac{\partial \Delta \phi}{\partial f} = 2\pi \Delta t \qquad (2)$$

Figure 1 illustrates the schematics of the setup used, in which intensity modulated light is split into two fibers. The total time delay the light undergoes in this configuration, due to the different optical paths, comprises the delay times of potential difference in the 50/50 splitter t_{50_x}, the fibers t_f and t_{spool}, and the electrical cables t_{e_x}. This means that the total time delay between the two paths can be expressed as:

$$\Delta t = (t_{50,1} + t_{f_{test}} - t_{50,2} - t_{spool}) + (t_{e1} - t_{e2}) \quad (3)$$

in which we are merely interested in the fiber that were measuring, t_{ftest}. To account for the split, electrical cabling and the spool, we introduce the parameters α and β which describe the systems inherent time delay. These parameters can be derived through a one-time calibration involving just two measurements (Δt_A and Δt_B), where during the measurement of Δt_B, only the ends of the fibers are switched to the other detector. When we write these two optical delays out, we get:

$$\Delta t_a = (t_{50,1} + t_f - t_{50,2} - t_{spool}) + (t_{e1} - t_{e2}) \quad (4)$$

$$\Delta t_b = (t_{50,2} + t_{spool} - t_{50,1} - t_f) + (t_{e1} - t_{e2}) \quad (5)$$

Due to cancellation of terms, α and β, can be determined through:

$$\frac{\Delta t_a + \Delta t_b}{2} = t_{e1} - t_{e2} = \beta \qquad (6)$$

$$\frac{\Delta t_a - \Delta t_b}{2} = t_f + t_{50,1} - t_{50,2} - t_{spool} \qquad (7)$$

$$= t_f + \alpha \qquad (8)$$

α is the system's offset due to differences in the 50/50 splitter, spool, and any patch cords connecting the sample fiber. β represents the offset caused by differences in the electrical cables. In this calibration procedure, t_f can and should be made zero by simply not connecting a measurement fiber in the system. After obtaining the calibration values for α and β, and measuring the phase difference over a wide frequency range, we obtain:

$$\frac{\partial \Delta \phi}{\partial f} = 2\pi(t_{f_{test}} + \alpha + \beta) \qquad (9)$$

The term $\frac{\partial \Delta \phi}{\partial f}$ can directly be determined from the phase meter by performing a linear fit on the frequency (f) and phase difference ($\Delta \phi$) data that is being stored by the phase meter. This means that almost no data processing, such as phase-unwrapping algorithms, is needed. Since the phase meter operates with a phase-locked-loop (PLL) where it integrates the voltage being send to the voltage controlled oscillator (VCO), it allows for phase tracking in cycles, which further simplifies the equation to:

$$\Delta t = \frac{\partial \Delta \phi}{\partial f} - \alpha - \beta \qquad (10)$$

2.2. Experimental setup

Central to our setup is the Moku:Lab (Liquid Instruments, USA), which has a built-in high-speed phasemeter. The Moku:Lab measures the voltage output of two detectors (DET02AFC, Thorlabs, USA). The laser used (LuxX.HSA1310-50, Omicron-Laserage Laserprodukte GmbH, Germany) allows for analog intensity modulation, controlled through an arbitrary waveform generator (AWG, T3AFG120, Teledyne Lecroy, Ireland) and its output is injected into an SMF28 fiber, after a fiber coupler (TN632R5A1, Thorlabs, USA) is then used to split the light into the two pahts.

2.3. Experimental conditions

A 200m SMF fiber was used to ensure a large enough difference between the two channels. During our tests, the light was modulated from 10MHz to 110MHz over a duration of 120 seconds, with an average power reaching the detectors of 5mW. No temperature control was used.

3. Results and Discussion

3.1. Accuracy

Figure 2 shows the measured time delays for different SM fibers of different lengths and indicates a linear relationship. Although the number of available fibers with distinct lengths was limited, an R2 and NRMSE of 0.99991 and 0.00256, respectively, give an indication of the accuracy of the proposed setup. It should be noted that the slope decreases for increasing lengths, as we measure the relative time delay with the 200m reference fiber, which decreases for longer fibers. Subsequent length conversion of the measured slopes depends on multiple factors and is explained in Section 3.3.
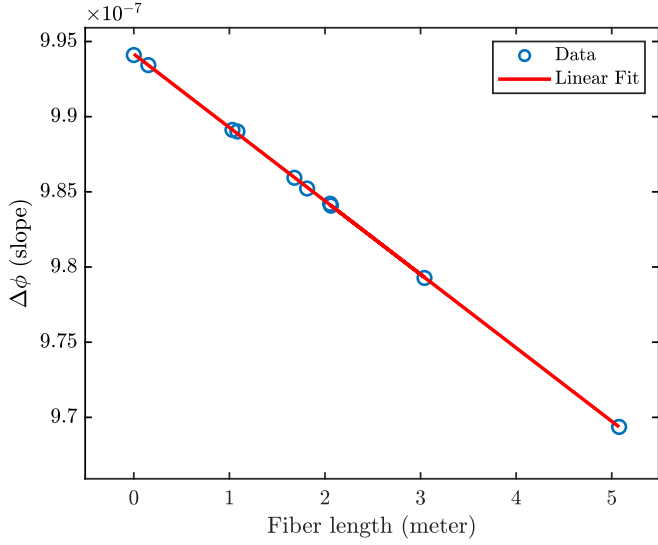
Figure 2: Measured time delay for different fibers

Figure 3: Temperature and length relationship

3.2. Precision

Since potential inaccuracies can be adjusted for through an additional correction parameter, a more important metric would be the precision. To assess the precision, we conducted continuous measurements over a long period and also monitored the ambient room temperature. These results are depicted in Figure 4 and indicate a total standard deviation (σ) of 2.3 mm, while there is also a period of over 4 hours with a notably low σ of 60 μm. We observed a strong correlation with temperature (Figure 3), which cannot be solely attributed to thermal effects on the optical fiber. Thermal expansion of undoped silica induces a delay time of 2 ps/km/K, whereas changes in the refractive index would contribute 37 ps/km/K [12], which is still a factor of ten smaller than the maximum variations observed. Due to the weak mechanical coupling between the fiber glass and the jacket, the contribution of the polymer jacket is not considered. However, the results suggest that there is a temperature-sensitive response within the system that has not yet been identified.

By applying linear regression to the empirical temperature-length relationship, we can smooth out the measured lengths, achieving a precision of $\sigma = 0.9$ mm. However, this method would not be practically useful, as it requires prolonged measurement times.

3.3. Length Conversion

The conversion of the measured time delays to lengths (z) is dependent on the propagation speed (V) within the fibers. The propagation speed can be determined through calibration measurements using two fibers with known but different lengths (z_{fiber}) through Eq. 11 and 12.

$$\frac{\partial \Delta \phi_1}{\partial f} = \frac{z_{50,1} + z_{\text{test},1} - z_{50,2} - z_{\text{spool}}}{V_{\text{fiber}}} + \frac{z_{e1} - z_{e2}}{V_{\text{cable}}} \quad (11)$$

$$\frac{\partial \Delta \phi_2}{\partial f} = \frac{z_{50,1} + z_{\text{test},2} - z_{50,2} - z_{\text{spool}}}{V_{\text{fiber}}} + \frac{z_{e1} - z_{e2}}{V_{\text{cable}}} \quad (12)$$
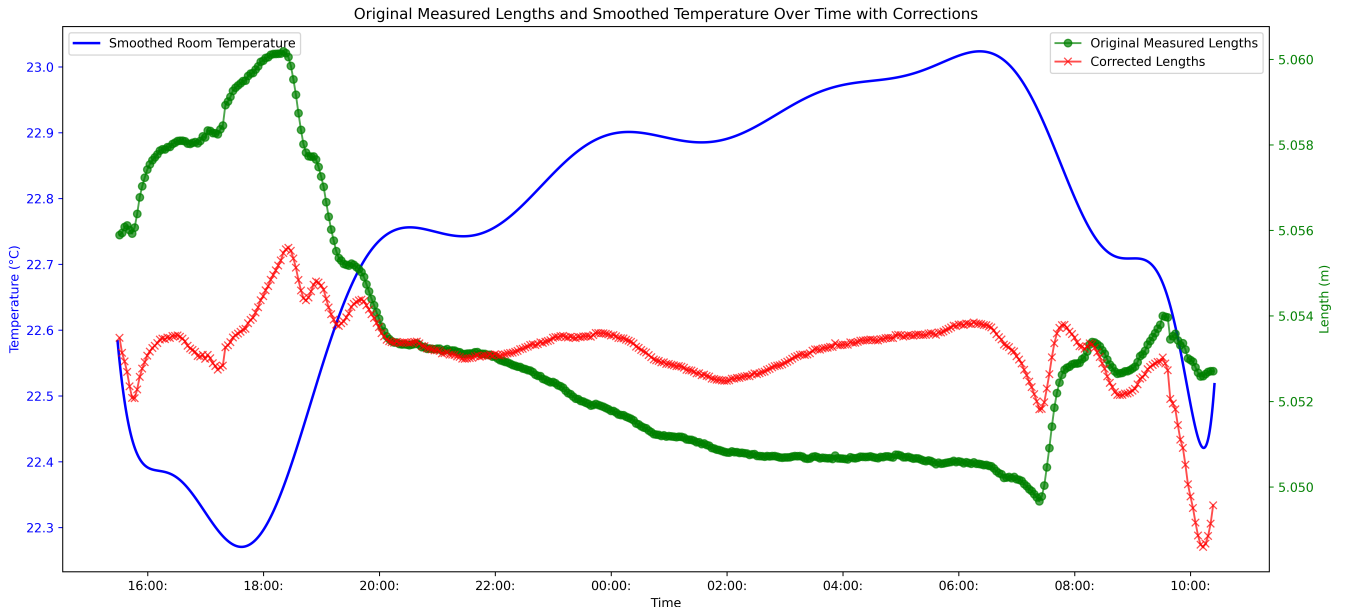

Figure 4: 434 lengths measurements and ambient room temperature which is used to empirically correct the measured lengths.

Then, as most terms cancel out by subtracting the two measurements, V_{fiber} is calculated as follows:

$$V_{\text{fiber}} = \frac{Z_{\text{fiber,1}} - Z_{\text{fiber,2}}}{\frac{\partial \Delta \phi_1}{\partial f} - \frac{\partial \Delta \phi_2}{\partial f}} \qquad (13)$$

One could also use the manufacturer-specified refractive index to derive the speed of light in the fiber. Still, it should be noted that this approach: I) comes with an uncertainty (if this information is available at all), and II) is greatly affected by temperature.

4. Conclusion

Despite unknown temperature effects, we report a simple and cost-effective method for measuring the length of optical fibers with a precision of 0.9 mm that surpasses traditional tape measurements. This makes our approach particularly appealing in settings such as optical labs, where the required components are often readily available and accurate knowledge of optical fiber lengths is essential, but manual tape measurements are impractical.

References

[1] Dankan G Veeranna et al. "Fiber Optic Communication: Evolution, Technology, Recent Developments, and Future Trends". In: *Modeling and Optimization of Optical Communication Networks* (2023), p. 163.

[2] Dianov E.M., Semjonov S.L., and Bufetov I.A. "New generation of optical fibres". In: *Quantum Electronics* 46 (1 Jan. 2016), pp. 1–10. ISSN: 1063-7818.

[3] Mohamed Elsherif et al. "Optical Fiber Sensors: Working Principle, Applications, and Limitations". In: *Advanced Photonics Research* 3 (11 Nov. 2022). ISSN: 2699-9293. DOI: 10.1002/ADPR.202100371.

[4] Byeong Ha Lee, Eun Jung Min, and Young Ho Kim. "Fiber-based optical coherence tomography for biomedical imaging, sensing, and precision measurements". In: *Optical Fiber Technology* 19 (6 Dec. 2013), pp. 729–740. ISSN: 1068-5200. DOI: 10.1016/J.YOFTE.2013.07.011.

[5] Ajaya Kumar Barik et al. "In vivo spectroscopy: optical fiber probes for clinical applications". In: *Expert Review of Medical Devices* 19 (9 2022), pp. 657–675. ISSN: 17452422. DOI: 10.1080/17434440.2022.2130046.

[6] Erik Bodtker, Bjarne Tromborg, and Jannik Mark. "Optical time domain reflectometer". In: *Applied optics* 16 (9 1977), pp. 70–89. ISSN: 1559-128X. DOI: 10.1364/AO.16.002375. URL: https://pubmed.ncbi.nlm.nih.gov/20168934/.

[7] Józef Kalisz. "Review of methods for time interval measurements with picosecond resolution". In: *Metrologia* 41 (1 Feb. 2004), pp. 17–32. DOI: 10.1088/0026-1394/41/1/004.

[8] R. Ulrich and W. Eickhoff. "Optical frequency-domain reflectometry in single-mode fibers". In: *Integrated Optics and Optical Fiber Communication (1981), paper WF3* (Apr. 1981), WF3. DOI: 10.1364/OFC.1981.WF3. URL: https://opg.optica.org/abstract.cfm?uri=OFC-1981-WF3.

[9] Shupeng Li et al. "Optical fiber transfer delay measurement based on phase-derived ranging". In: *IEEE Photonics Technology Letters* 31 (16 Aug. 2019). super close to ours, pp. 1351–1354. ISSN: 19410174. DOI: 10.1109/LPT.2019.2926508.

[10] Xinxin Huang et al. "Time Delay Measurement in Optical Fibers Based on Phase Detection". In: *2018 IEEE 3rd Optoelectronics Global Conference (OGC)*. 2018, pp. 130–134. DOI: 10.1109/OGC.2018.8529980.

[11] Shupeng Li et al. "High-Accuracy Optical Fiber Transfer Delay Measurement Using Fiber-Optic Microwave Interferometry". In: *JOURNAL OF LIGHTWAVE TECHNOLOGY* 39 (2 2021). Same authors as 2019 article, but use interferemotry. Basically same principle. DOI: 10.1109/JLT.2020.3033280. URL: https://www.ieee.org/publications/rights/index.html.

[12] American Institute of Physics. *Handbook*. Maidenhead, England: McGraw Hill Higher Education, 1972, p. 2200. ISBN: 9780070014855.

8 General Discussion

8.1 Achievement of research objectives

The main goal of this research was to investigate potential methods for overcoming glare, which would pave the way for quantitative imaging spectroscopy (iSFR) in a multimodal endoscopic OCT setup. The core hypothesis was that we could model and approximate the unwanted glare as a simple Fresnel reflection (Eq. 10) and incorporate it into existing models to relate the acquired spectral data to the optical and biological properties of the tissue. This motivated the investigation in Chapter 3 whether the single fiber reflectance (SFR) spectroscopy model could be applied to the geometry and dimensions of its novel imaging counterpart, iSFR. Monte Carlo (MC) simulations yielded results different from those predicted by current models, indicating that existing SFR models are unsuitable for iSFR. These MC simulations were part of a framework designed to run a vast number of simulations with post-simulation flexibility, facilitating future iSFR model development.

As a workaround, we developed and tested an algorithm in Chapter 4 incorporating glare. Although the analysis still utilized the current SFR model and spectral data, assuming that future iSFR models would exhibit similar behavior in terms of fit parameters and non-linearity, the results should also hold for iSFR models. The analysis demonstrated that by modeling glare as Fresnel reflections, SFR spectra can be distorted with glare and noise up to 15dB SNR, while still achieving robust and accurate fit results. This suggests that it may be possible to incorporate glare as a few additional fitting parameters in a future iSFR model.

Unfortunately, the experimental validation in Chapter 5 of the developed algorithm, using very simplified homogeneous phantoms that did not require an actual iSFR model, was inconclusive due to high distortions in the spectra of pixels affected by glare, which did not adhere to the Fresnel equation. Chapter 6 initially aimed to further test the benchtop system by exploring a relationship between a specific signal characteristic in OCT and the glare present in iSFR. However, due to the limited time remaining for this analysis, newly identified issues with our phantom, and the distinctiveness between the two modalities, it was decided to designate this as future work and only present the inconclusive results from a preliminary measurement set. Nevertheless, the analysis in both Chapters 5 and 6 provided new insights into this multimodal system's signal characteristics and identified areas for improvement.

8.2 Limitations

The central assumption underpinning the conclusions drawn about the possibility of including glare as fitting parameters is that iSFR models would exhibit similar behavior to SFR models. In Chapter 4, only SFR-simulated reflectance spectra of two tissue types—skin and soft tissue—were tested without considering iSFR spectra. The rationale behind this assumption is that an iSFR model would likely be constructed similarly but optimized for conditions where the numerical aperture (NA), and thus photon scattering events and partial path length, is much lower. This could result in a derivation similar to that outlined in Appendix A. However, much remains unknown; for instance, whether the inherently lower photon count in iSFR affects sensitivity to specific fitting parameters or if the two waveguides of the double-clad fiber (DCF) are of sufficient sizes to support MD-iSFR analysis.

Additionally, fitting noisy data becomes more challenging when glare in iSFR can be a thousand times stronger compared to being roughly ten times as strong in SFR. Spectral features of the SFR spectra remain visible under maximal glare, but in iSFR, almost nothing remains. We show that it is still sufficient to produce accurate fits in the absence of noise, but one could imagine that these minimal remaining spectral features in glare-distorted pixels could be overwhelmed by noise. In a preliminary check, we observed improved performance as the spectral resolution increased. Although this is possible with synthetic calculated spectra, spectrometers generally achieve nm resolution at most, indicating the potential for spectral averaging or other pre-processing techniques once more.

Another limitation of the conducted research was the lack of experimental validation, mostly due to the low quality of obtained spectra as described in Section 5.4. In addition to still needing to identify and correct the cause for the distorted reflectance spectra in highly glare-affected pixels, we also observed a high dark spectrum for cladding illumination, where most of the light picked up by the spectrometer was an internal back reflection. Reducing internal back-reflections could further enhance the sensitivity and quality of iSFR spectra. Furthermore, we were restricted to a spectral bandwidth of 450 to 950 nm instead of the total 450 to 1700 nm, as demonstrated previously, due to system defects. Also, artifacts were present in the OCT system for most of the research period, which limited the time available for better-controlled experiments

and thorough analysis in Chapter 6. However, this issue did lead to the development of a newly designed scanner head and Fiber Length Measurement System (FLMS) detailed in Chapter 7.

8.3 Future outlook

The next priority is developing an iSFR model that should include glare to a certain degree. The current benchtop system can produce reflectance maps for a broadband spectrum of light, which could already reveal additional relative biochemical information alongside the high-resolution OCT images. However, quantifying certain scattering properties or chromophores is essential in advancing the development of this multimodal endoscope toward cancer detection. If modeling the glare as we propose does not result in stable and accurate fit results due to the aforementioned limitations, the focus should shift towards pre-processing techniques as outlined in [67]. Multiple data-processing techniques have already been applied in hyperspectral imaging to reduce the variability between spectra due to glare. Although these methods would not seamlessly apply for iSFR spectra, in which, due to the high levels of glare that are possible, the spectral shape and features get absorbed instead of merely offset, they do offer a proper starting point for tissue classification despite glare being present up to a certain degree.

An increasing focus on endoscopic imaging spectroscopy for tissue classification, resulting in a deeper understanding of tissue physiology, could facilitate a transition from broad-spectrum to multispectral imaging techniques while still capturing useful biological and optical properties. Such a shift could enhance image acquisition speed [95], given that broadband spectroscopes operate relatively slowly. For context, the system described in Chapter 5 operated at a sampling frequency of 250 Hz, constrained by the spectrometer's capacity, whereas the OCT system achieves a scanning rate of 50 kHz per A-line.

To achieve (near) real-time imaging, significant advancements must be made in processing the acquired spectral data. It is important to note that a relatively small image of 256×256 pixels, acquired over a wavelength range from 450 nm to 1700 nm with a resolution of 1 nanometer, already constitutes a matrix of over 85 million data points. Moreover, solving the optimization problem pixel by pixel for just a few centimeters of the esophageal tissue can take days to process as one wants to utilize the full fine spectral resolution. Fortunately, the algorithm has the potential to be massively parallelized using GPU accelerated and/or cloud computing allowing for high core-count parallel processing. This technique is becoming increasingly popular in medical imaging due to the rise of Artificial Intelligence (AI) [96]. AI itself could also accelerate image processing in iSFR as larger datasets become available. A less black box approach would involve using spatial averaging or clustering methods, assuming that the tissue at our imaging scale is mostly homogeneous with relatively slow transitions between pixels. This would not only accelerate processing but also enhance the model's robustness.

The detection possibilities extend beyond just esophageal cancer, as the multimodal, aberration-free, and back-reflection-free endoscope can be used for multiple tubular organs, and spectroscopy has the potential to assist in classifying various types of cancer [35, 97]. A systematic validation process is essential, given its potential for widespread clinical use. Before clinical trials, an intermediate step in which performance is benchmarked against histology examinations is the standard route. Due to the fine spatial resolution of both the OCT and iSFR, it is crucial to compare the same tissue spots for accurate benchmarking. Additionally, it is extremely valuable to mark regions during real-time imaging to better guide biopsies or resections during conventional subsequent white light endoscopy. Both can be achieved through laser-marking techniques, which have already been successfully tested in multimodal endoscopic OCT probes [98, 99]. Therefore, they present themselves as logical candidates for incorporation into the current system. Moreover, although double-clad fibers (DCF) inherently enable a multimodal approach, the capabilities should not be limited to what DCFs and accompanying couplers can achieve. A variety of multiplexing techniques exist that could enable the integration of additional optical methods. However, more research directed at optical detection methods for cancer should guide us in determining which optical techniques offer the most added value.

9   General Conclusion

This research explored the possibility of incorporating glare into an optimization algorithm to retrieve optical and biological properties from reflectance spectra despite being affected by noise and an unknown amount of glare. We found that existing SFR models do not seamlessly adapt to the smaller iSFR geometries, which motivated our analysis of SFR spectra. By modeling glare as a Fresnel reflection, we demonstrated that it is possible to maintain the desired accuracy up to an SNR of 15 dB.

Despite eliminating potential sources of uncertainty, experimental validation of the developed algorithm on iSFR spectra acquired by the benchtop system was not feasible due to an unknown factor causing high distortion in spectra affected by glare. Furthermore, we proposed a methodology and additional signal characteristics that could be useful in establishing a relationship between OCT and glare in iSFR; however, experimental validation was again limited.

Nevertheless, our findings support the potential for integrating glare into imaging spectroscopy models, thereby underscoring the value of developing iSFR models compatible with DCFs. Such a model would enable the quantification of biological and optical properties in the high-resolution multimodal endoscopic OCT system, advancing its diagnostic capabilities. Additionally, our research has identified several potential improvements and considerations for future iSFR model development. The OCT component of our study not only provided deeper insights into the experimental integration of the two modalities but also introduced a novel method for measuring the length of optical fibers.

A SFR Model

From Post et al. [54]:

The reflectance is modeled as the sum of a semiballistic reflectance $R_{\text{SFR,sb}}$ and diffuse reflectance $R_{\text{SFR,dif}}$:

$$R_{\text{SFR}} = R_{\text{SFR,sb}} + R_{\text{SFR,dif}} = (1 + X) \cdot R_{\text{SFR,dif}} \tag{16}$$

where X is the ratio between the semiballistic and diffuse reflectance:

$$X = \frac{R_{\text{SFR,sb}}}{R_{\text{SFR,dif}}} \tag{17}$$

The diffuse reflectance $R_{\text{SFR,dif}}$ equals the collection efficiency of the fiber η_c times the fraction of diffuse photons that reach the fiber face R_{dif}:

$$R_{\text{SFR,dif}} = \eta_c \cdot R_{\text{dif}} \tag{18}$$

where $\eta_c = (\text{NA}/n)^2 \cdot 1.11$, NA is the fiber numerical aperture and n is the tissue refractive index. The fraction of diffuse photons that reach the fiber is calculated as [57]:

$$R_{\text{dif}}(\mu_s', \mu_a, d_f) = \frac{\pi}{4} \cdot d_f^2 \cdot \int_0^\infty R(p, \mu_s', \mu_a) \cdot \rho(p, d_f) dp \tag{19}$$

where μ_s' is the reduced scattering coefficient, μ_a the absorption coefficient and d_f the fiber diameter. $R(p, \mu_s', \mu_a)$ is the diffuse reflectance versus radial distance p for a pencil beam illumination using the Extended Boundary Condition as proposed by Farrell et al. [100]:

$$R(p, \mu_s', \mu_a) = \frac{a'}{4\pi} \left[\frac{1}{(z_0' + \mu_{eff}'^{-1})^2 + r_1^2} \cdot e^{-\mu_{eff}' r_1} + \frac{1}{(z_0 + 2z_b + \mu_{eff}'^{-1})^2 + r_2^2} \cdot e^{-\mu_{eff}' r_2} \right] \tag{20}$$

where $a' = \frac{\mu_s'}{(\mu_s' + \mu_a)}$; $z_0' = \frac{1}{\mu_s'}$; $\mu_{eff} = \sqrt{3\mu_a(\mu_s' + \mu_a)}$; $r_1 = \sqrt{(z_0' + \mu_{eff}'^{-1})^2 + p^2}$; $r_2 = \sqrt{(z_0 + 2z_b + \mu_{eff}'^{-1})^2 + p^2}$; and A is a parameter that depends on the refractive index mismatch between the fiber and the tissue [41]. The integral of the diffuse reflectance versus Radial distance is performed over the probability density function of distances over the fiber face $p(\rho)$:

$$p(\rho) = \frac{16\rho}{\pi d_f^2} \cos^{-1}\left(\frac{\rho}{d_f}\right) - \frac{16}{\pi d_f} \sqrt{1 - \left(\frac{\rho}{d_f}\right)^2} \tag{21}$$

The parameter p_{sb} is used to model the semiballistic contribution to the reflectance [53], which is related to the tissue phase function $p(\theta)$ as:

$$p_{sb} = \frac{p_r(1°)}{1 - p_r(23°)} \tag{22}$$

where $p_r(1°)$ is the probability of a photon undergoing a scattering event between 0 and 1 degrees in the backward direction. This probability equals the integral over the phase function over 1 degree in the backward direction:

$$p_r(1°) = 2\pi \int_{-1°}^{0} p(\theta) \sin\theta d\theta \tag{23}$$

$p_r(23°)$ is the probability of a photon undergoing a scattering event between 0 and 23 degrees in the forward direction:

$$p_r(23°) = 2\pi \int_{0}^{23°} p(\theta) \sin\theta d\theta \tag{24}$$

X – in the absence of absorption – can be modelled as a function of p_{sb} and $\mu_s' d_f$ [53]:

$$X = 3046 \left(\frac{p_{sb}}{(\mu_s' d_f)^2}\right)^{0.748} \tag{25}$$

To take absorption into account, the reflectance can be written as the product of the reflectance in the absence of absorption (R_0) and the integral of the photon path length distribution $p(l)$ weighted by the Beer-Lambert law:

$$R(\mu_a) = R_0 \int_0^\infty p(l)e^{-\mu_a l}dl \tag{26}$$

$$X = 3046 \left(\frac{p_{sb}}{(\mu_s' d_f)^2}\right)^{0.748} \cdot e^{-\left(\frac{b_1 \mu_a}{\mu_s'}\right)^{b_2}} \tag{27}$$

Where the coefficient were found as optimal by testing the accuracy over a wide variety of phase functions and optical properties.

B   AI Statement

During the preparation of this work, the authors used ChatGPT 3.5 and Grammarly to correct **their own generated** text in terms of grammar, spelling, and sometimes fluency. ChatGPT was also used to assist in coding in Python, Matlab, and LabView, but not to generate text from scratch. After using these tools, the authors reviewed and edited the content as needed and take full responsibility for the content of the work.

References

[1] A. Giardino et al. "Role of Imaging in the Era of Precision Medicine". In: *Academic Radiology* 24.5 (2017), pp. 639–649. DOI: https://doi.org/10.1016/j.acra.2016.11.021.

[2] S. Hussain et al. "Modern Diagnostic Imaging Technique Applications and Risk Factors in the Medical Field: A Review". In: *BioMed Research International* (2022), pp. 51–64. DOI: 10.1155/2022/5164970.

[3] K. Doi. "Diagnostic imaging over the last 50 years: research and development in medical imaging science and technology". In: *Physics in Medicine Biology* 51.13 (2006), R5. DOI: 10.1088/0031-9155/51/13/R02.

[4] S. Aumann et al. "Optical Coherence Tomography (OCT): Principle and Technical Realization". In: *High Resolution Imaging in Microscopy and Ophthalmology: New Frontiers in Biomedical Optics*. Ed. by J.F. Bille. Cham: Springer International Publishing, 2019, pp. 59–85. ISBN: 978-3-030-16638-0. DOI: 10.1007/978-3-030-16638-0_3. URL: https://doi.org/10.1007/978-3-030-16638-0_3.

[5] D. Huang et al. "Optical coherence tomography". In: *Science* 254.5035 (1991), pp. 1178–81. DOI: 10.1126/science.1957169.

[6] N. Minakaran et al. "Optical coherence tomography (OCT) in neuro-ophthalmology". In: *Eye* 35.1 (2021), pp. 17–32. DOI: 10.1038/s41433-020-01288-x.

[7] J. Wang, Y. Xu, and S.A. Boppart. "Review of optical coherence tomography in oncology". In: *J Biomed Opt* 22.12 (2017), pp. 1–23. DOI: 10.1117/1.Jbo.22.12.121711.

[8] N. Acharya et al. "Types of Optical Coherence Tomography for Cancer Diagnosis: A Systematic Review". In: *Journal of Biomedical Photonics Engineering* 8 (2022), p. 010201. DOI: 10.18287/JBPE22.08.010201.

[9] B.J. Vakoc et al. "Cancer imaging by optical coherence tomography: preclinical progress and clinical potential". In: *Nature Reviews Cancer* 12.5 (2012), pp. 363–368. DOI: 10.1038/nrc3235.

[10] M.J. Gora et al. "Endoscopic optical coherence tomography: technologies and clinical applications [Invited]". In: *Biomedical Optics Express* 8.5 (2017), pp. 2405–2444. DOI: 10.1364/BOE.8.002405.

[11] A.L. Rainer et al. "Enhanced medical diagnosis for dOCTors: a perspective of optical coherence tomography". In: *Journal of Biomedical Optics* 26.10 (2021), p. 100601. DOI: 10.1117/1.JBO.26.10.100601.

[12] D. Wolfgang et al. "Optical coherence tomography today: speed, contrast, and multimodality". In: *Journal of Biomedical Optics* 19.7 (2014), p. 071412. DOI: 10.1117/1.JBO.19.7.071412.

[13] X. Attendu. "Advancements in Multimodal Endoscopic Optical Coherence Tomography: Novel Hardware, Software, and Optical Strategies". Polytechnique Montréal. Thesis. 2022. URL: https://publications.polymtl.ca/10561/.

[14] M.F. Vitha. *Spectroscopy: Principles and Instrumentation*. Wiley, 2018, Chapter 1: Fundamentals. ISBN: 9781119436645. URL: https://books.google.nl/books?id=uWhvDwAAQBAJ.

[15] A. Steyerl, S.S. Malik, and L.R. Iyengar. "Specular and diffuse reflection and refraction at surfaces". In: *Physica B: Condensed Matter* 173.1 (1991), pp. 47–64. DOI: https://doi.org/10.1016/0921-4526(91)90034-C.

[16] B. van Ginneken, M. Stavridi, and J.J. Koenderink. "Diffuse and Specular Reflectance from Rough Surfaces". In: *Applied Optics* 37.1 (1998), pp. 130–139. DOI: 10.1364/AO.37.000130.

[17] M. Sylvain. "Diffuse reflection by rough surfaces: an introduction". In: *Comptes Rendus Physique* 6.6 (2005), pp. 663–674. DOI: https://doi.org/10.1016/j.crhy.2005.06.014.

[18] G. Gianini et al. "Glare removal as an ill-conditioned problem". In: *Journal of Electronic Imaging* 28.6 (2019), p. 063014.

[19] D.J. Uhlenhopp et al. "Epidemiology of esophageal cancer: update in global trends, etiology and risk factors". In: *Clin J Gastroenterol* 13.6 (2020), pp. 1010–1021. DOI: 10.1007/s12328-020-01237-x.

[20] M.A. Eloubeidi and D. Provenzale. "Does this patient have Barrett's esophagus? The utility of predicting Barrett's esophagus at the index endoscopy". In: *Am J Gastroenterol* 94.4 (1999), pp. 937–43. DOI: 10.1111/j.1572-0241.1999.990_m.x.

[21] P.J. de Jonge et al. "Barrett's oesophagus: epidemiology, cancer risk and implications for management". In: *Gut* 63.1 (2014), pp. 191–202. DOI: 10.1136/gutjnl-2013-305490.

[22] B.J. Vakoc et al. "Comprehensive esophageal microscopy by using optical frequency–domain imaging (with video)". In: *Gastrointestinal Endoscopy* 65.6 (2007), pp. 898–905. DOI: https://doi.org/10.1016/j.gie.2006.08.009.

[23] A. Wartak et al. "Dual-modality optical coherence tomography and fluorescence tethered capsule endomicroscopy". In: *Biomed Opt Express* 12.7 (2021), pp. 4308–4323. DOI: 10.1364/boe.422453.

[24] J. Mavadia et al. "An all-fiber-optic endoscopy platform for simultaneous OCT and fluorescence imaging". In: *Biomed Opt Express* 3.11 (2012), pp. 2851–9. DOI: 10.1364/boe.3.002851.

[25] W. Andreas et al. "Multimodality optical coherence tomography based tethered capsule endomicroscopy for upper gastrointestinal tract imaging". In: *Proc.SPIE*. Vol. 11630, 116300P. DOI: 10.1117/12.2582536. URL: https://doi.org/10.1117/12.2582536.

[26] D.R. Kohli et al. "Performance characteristics of optical coherence tomography in assessment of Barrett's esophagus and esophageal cancer: systematic review". In: *Dis Esophagus* 30.11 (2017), pp. 1–8. DOI: 10.1093/dote/dox049.

[27] F. Yousef et al. "The Incidence of Esophageal Cancer and High-Grade Dysplasia in Barrett's Esophagus: A Systematic Review and Meta-Analysis". In: *American Journal of Epidemiology* 168.3 (2008), pp. 237–249. DOI: 10.1093/aje/kwn121.

[28] H.D. Appelman et al. "Progression of esophageal dysplasia to cancer". In: *Annals of the New York Academy of Sciences* 1325.1 (2014), pp. 96–107. DOI: https://doi.org/10.1111/nyas.12523.

[29] S. Rogalla and C.H. Contag. "Early Cancer Detection at the Epithelial Surface". In: *The Cancer Journal* 21.3 (2015).

[30] J.R. Mourant et al. "Evidence of intrinsic differences in the light scattering properties of tumorigenic and nontumorigenic cells". In: *Cancer* 84.6 (1998), pp. 366–74.

[31] G. Zonios et al. "Diffuse reflectance spectroscopy of human adenomatous colon polyps in vivo". In: *Appl Opt* 38.31 (1999), pp. 6628–37. DOI: 10.1364/ao.38.006628.

[32] N.M. Yvette et al. "Reflectance spectroscopy for in vivo detection of cervical precancer". In: *Journal of Biomedical Optics* 7.4 (2002), pp. 587–594. DOI: 10.1117/1.1502675.

[33] M.S. Nogueira et al. "Evaluation of wavelength ranges and tissue depth probed by diffuse reflectance spectroscopy for colorectal cancer detection". In: *Scientific Reports* 11.1 (2021), p. 798. DOI: 10.1038/s41598-020-79517-2.

[34] M. Witteveen et al. "Opportunities and pitfalls in (sub)diffuse reflectance spectroscopy". In: *Frontiers in Photonics* 3 (2022). DOI: 10.3389/fphot.2022.964719.

[35] K. Sokolov, M. Follen, and R. Richards-Kortum. "Optical spectroscopy for detection of neoplasia". In: *Current Opinion in Chemical Biology* 6.5 (2002), pp. 651–658. DOI: https://doi.org/10.1016/S1367-5931(02)00381-2.

[36] A.L. Post et al. "Toward improved endoscopic surveillance with multidiameter single fiber reflectance spectroscopy in patients with Barrett's esophagus". In: *Journal of Biophotonics* 14.4 (2021), e202000351. DOI: https://doi.org/10.1002/jbio.202000351.

[37] L. van Manen et al. "Single fiber reflectance spectroscopy for pancreatic cancer detection during endoscopic ultrasound guided fine needle biopsy: a prospective cohort study". In: *Int J Med Sci* 19.2 (2022), pp. 205–212. DOI: 10.7150/ijms.65364.

[38] Y. Li et al. "Multimodality endoscopic optical coherence tomography and fluorescence imaging technology for visualization of layered architecture and subsurface microvasculature". In: *Opt Lett* 43.9 (2018), pp. 2074–2077. DOI: 10.1364/ol.43.002074.

[39] D. Lorenser et al. "Dual-modality needle probe for combined fluorescence imaging and three-dimensional optical coherence tomography". In: *Optics Letters* 38.3 (2013), pp. 266–268. DOI: 10.1364/OL.38.000266.

[40] S.Y. Ryu et al. "Combined system of optical coherence tomography and fluorescence spectroscopy based on double-cladding fiber". In: *Optics Letters* 33.20 (2008), pp. 2347–2349. DOI: 10.1364/OL.33.002347.

[41] D.P. Popescu et al. "Optical coherence tomography: fundamental principles, instrumental designs and biomedical applications". In: *Biophys Rev* 3.3 (2011), p. 155. DOI: 10.1007/s12551-011-0054-7.

[42] M. Born and E. Wolf. *Principles of optics*. 7th ed. Cambridge, England: Cambridge University Press, 2019, p. 992. ISBN: 9781108477437.

[43]   Science Photo Library. *Normal retina OCT scan*. URL: https://www.sciencephoto.com/media/690599/view/normal-retina-oct-scan.

[44]   C. Boudoux. *Fundamentals of biomedical optics*. 2017. ISBN: 9781366451194.

[45]   J.A. Izatt and M.A. Choma. "Theory of Optical Coherence Tomography". In: *Optical Coherence Tomography: Technology and Applications*. Ed. by W. Drexler and J.G. Fujimoto. Berlin, Heidelberg: Springer Berlin Heidelberg, 2008, pp. 47–72. ISBN: 978-3-540-77550-8. DOI: 10.1007/978-3-540-77550-8_2. URL: https://doi.org/10.1007/978-3-540-77550-8_2.

[46]   E.A. Rank et al. "Miniaturizing optical coherence tomography". In: *Translational Biophotonics* 4.1-2 (2022), e202100007. DOI: https://doi.org/10.1002/tbio.202100007.

[47]   Y. Zahid et al. "Methods and application areas of endoscopic optical coherence tomography". In: *Journal of Biomedical Optics* 11.6 (2006), p. 063001. DOI: 10.1117/1.2400214.

[48]   J.M. Zara and C.A. Lingley-Papadopoulos. "Endoscopic OCT Approaches Toward Cancer Diagnosis". In: *IEEE Journal of Selected Topics in Quantum Electronics* 14.1 (2008), pp. 70–81. DOI: 10.1109/JSTQE.2007.912020.

[49]   H.S. Nam and H. Yoo. "Spectroscopic optical coherence tomography: A review of concepts and biomedical applications". In: *Applied Spectroscopy Reviews* 53.2-4 (2018), pp. 91–111. DOI: 10.1080/05704928.2017.1324876.

[50]   B. Braaf et al. "OCT-Based Velocimetry for Blood Flow Quantification". In: *High Resolution Imaging in Microscopy and Ophthalmology: New Frontiers in Biomedical Optics*. Ed. by J.F. Bille. Cham (CH): Springer Copyright 2019, The Author(s)., 2019, pp. 161–79. DOI: 10.1007/978-3-030-16638-0_7.

[51]   G. Kortüm, W. Braun, and G. Herzog. "Principles and Techniques of Diffuse-Reflectance Spectroscopy". In: *Angewandte Chemie International Edition in English* 2.7 (1963), pp. 333–341. DOI: https://doi.org/10.1002/anie.196303331.

[52]   T.J. Farrell, M.S. Patterson, and B. Wilson. "A diffusion theory model of spatially resolved, steady-state diffuse reflectance for the noninvasive determination of tissue optical properties in vivo". In: *Medical Physics* 19.4 (1992), pp. 879–888. DOI: https://doi.org/10.1118/1.596777.

[53]   A.L. Post et al. "Subdiffuse scattering model for single fiber reflectance spectroscopy". In: *Journal of Biomedical Optics* 25.1 (2020), p. 015001. DOI: 10.1117/1.JBO.25.1.015001.

[54]   A.L. Post et al. "Subdiffuse scattering and absorption model for single fiber reflectance spectroscopy". In: *Biomedical Optics Express* 11 (2020), p. 6620. DOI: 10.1364/BOE.402466.

[55]   S.C. Kanick et al. "Monte Carlo analysis of single fiber reflectance spectroscopy: photon path length and sampling depth". In: *Phys Med Biol* 54.22 (2009), pp. 6991–7008. DOI: 10.1088/0031-9155/54/22/016.

[56]   S.C. Kanick et al. "Method to quantitatively estimate wavelength-dependent scattering properties from multidiameter single fiber reflectance spectra measured in a turbid medium". In: *Opt Lett* 36.15 (2011), pp. 2997–9. DOI: 10.1364/ol.36.002997.

[57]   D.J. Faber et al. "Analytical model for diffuse reflectance in single fiber reflectance spectroscopy". In: *Optics Letters* 45.7 (2020), pp. 2078–2081. DOI: 10.1364/OL.385845.

[58]   Z. Caigang and L. Quan. "Review of Monte Carlo modeling of light transport in tissues". In: *Journal of Biomedical Optics* 18.5 (2013), p. 050902. DOI: 10.1117/1.JBO.18.5.050902.

[59]   S.E. Skipetrov and S.S. Chesnokov. "Analysis, by the Monte Carlo method, of the validity of the diffusion approximation in a study of dynamic multiple scattering of light in randomly inhomogeneous media". In: *Quantum Electronics* 28.8 (1998), p. 733. DOI: 10.1070/QE1998v028n08ABEH001313.

[60]   Q. Fang and D.A. Boas. "Monte Carlo Simulation of Photon Migration in 3D Turbid Media Accelerated by Graphics Processing Units". In: *Optics Express* 17.22 (2009), pp. 20178–20190. DOI: 10.1364/OE.17.020178.

[61]   S.L. Jacques. "Optical properties of biological tissues: a review". In: *Phys Med Biol* 58.11 (2013), R37–61. DOI: 10.1088/0031-9155/58/11/r37.

[62]   R. García-Pelayo. "Distribution of distance in the spheroid". In: *Journal of Physics A: Mathematical and General* 38.16 (2005), p. 3475. DOI: 10.1088/0305-4470/38/16/001.

[63]   A. Sassaroli and F. Martelli. "Equivalence of four Monte Carlo methods for photon migration in turbid media". In: *Journal of the Optical Society of America A* 29.10 (2012), pp. 2110–2117. DOI: 10.1364/JOSAA.29.002110.

[64] D. Beasley, D.R. Bull, and R.R. Martin. "An overview of genetic algorithms: Part 1". In: 1993.

[65] S. Taghiyeh and J. Xu. "A new particle swarm optimization algorithm for noisy optimization problems". In: *Swarm Intelligence* 10.3 (2016), pp. 161–192. DOI: 10.1007/s11721-016-0125-2.

[66] A. Suppapitnarm et al. "A SIMULATED ANNEALING ALGORITHM FOR MULTIOBJECTIVE OPTIMIZATION". In: *Engineering Optimization* 33.1 (2000), pp. 59–85. DOI: 10.1080/03052150008940911.

[67] M. Witteveen et al. "Comparison of preprocessing techniques to reduce nontissue-related variations in hyperspectral reflectance imaging". In: *J Biomed Opt* 27.10 (2022). DOI: 10.1117/1.Jbo.27.10.106003.

[68] R. Michels, F. Foschum, and A. Kienle. "Optical properties of fat emulsions". In: *Optics Express* 16.8 (2008), pp. 5907–5925. DOI: 10.1364/OE.16.005907.

[69] K. Beaudette et al. "Radiometric model for coaxial single- and multimode optical emission from double-clad fiber". In: *Applied Optics* 57.5 (2018), pp. 1110–1118. DOI: 10.1364/AO.57.001110.

[70] X. Attendu et al. *Stabilized single-fiber reflectance spectroscopy using wideband multimode circulators.* Vol. PC12831. SPIE BiOS. SPIE, 2024. URL: https://doi.org/10.1117/12.3003093.

[71] I. Thormählen, J. Straub, and U. Grigull. "Refractive Index of Water and Its Dependence on Wavelength, Temperature, and Density". In: *Journal of Physical and Chemical Reference Data* 14.4 (1985), pp. 933–945. DOI: 10.1063/1.555743.

[72] B. Aernouts et al. "Dependent scattering in Intralipid® phantoms in the 600-1850 nm range". In: *Optics Express* 22.5 (2014), pp. 6086–6098. DOI: 10.1364/OE.22.006086.

[73] N. Bodenschatz et al. "Surface layering properties of Intralipid phantoms". In: *Phys Med Biol* 60.3 (2015), pp. 1171–83. DOI: 10.1088/0031-9155/60/3/1171.

[74] T. Koopman. "Advancing Glare Management in a Combined OCT i SFR System: Non Quantitative Detection Method and Multifaceted Glare Analyses". Thesis. 2024.

[75] X. Attendu et al. "Simple and robust calibration procedure for k-linearization and dispersion compensation in optical coherence tomography". In: *Journal of Biomedical Optics* 24.5 (2019), p. 056001. DOI: 10.1117/1.JBO.24.5.056001.

[76] K. Basak, M. Manjunatha, and P.K. Dutta. "Review of laser speckle-based analysis in medical imaging". In: *Medical Biological Engineering Computing* 50.6 (2012), pp. 547–558. DOI: 10.1007/s11517-012-0902-z.

[77] H. Wido et al. "Clinical applications of laser speckle contrast imaging: a review". In: *Journal of Biomedical Optics* 24.8 (2019), p. 080901. DOI: 10.1117/1.JBO.24.8.080901.

[78] M.-q. Shao et al. "A review of surface roughness measurements based on laser speckle method". In: *Journal of Iron and Steel Research International* 30.10 (2023), pp. 1897–1915. DOI: 10.1007/s42243-023-00930-8.

[79] M.S. Joseph, S.H. Xiang, and Y. Kin Man. "Speckle in optical coherence tomography: an overview". In: *Proc.SPIE.* Vol. 3726, pp. 450–461. DOI: 10.1117/12.341428. URL: https://doi.org/10.1117/12.341428.

[80] Y. Ma et al. "Speckle noise reduction in optical coherence tomography images based on edge-sensitive cGAN". In: *Biomed Opt Express* 9.11 (2018), pp. 5129–5146. DOI: 10.1364/boe.9.005129.

[81] V.B. Silva et al. "Signal-carrying speckle in optical coherence tomography: a methodological review on biomedical applications". In: *J Biomed Opt* 27.3 (2022). DOI: 10.1117/1.Jbo.27.3.030901.

[82] B.S. Vania et al. "Signal-carrying speckle in optical coherence tomography: a methodological review on biomedical applications". In: *Journal of Biomedical Optics* 27.3 (2022), p. 030901. DOI: 10.1117/1.JBO.27.3.030901.

[83] S. Askaruly et al. "Quantitative Evaluation of Skin Surface Roughness Using Optical Coherence Tomography In Vivo". In: *IEEE Journal of Selected Topics in Quantum Electronics* 25.1 (2019), pp. 1–8. DOI: 10.1109/JSTQE.2018.2873489.

[84] M.A. Marcello et al. "Roughness measurement methodology according to DIN 4768 using optical coherence tomography (OCT)". In: *Proc.SPIE.* Vol. 7390, 73900Z. DOI: 10.1117/12.827748. URL: https://doi.org/10.1117/12.827748.

[85] H. Gheorghe et al. "Roughness measurements using optical coherence tomography: a preliminary study". In: *Proc.SPIE.* Vol. 10831, 108310S. DOI: 10.1117/12.2282807. URL: https://doi.org/10.1117/12.2282807.

[86] T. Tkaczyk, K. Gossage, and J. Barton. "Speckle image properties in optical coherence tomography". In: *Proceedings of SPIE - The International Society for Optical Engineering* 4619 (2002). DOI: `10.1117/12.470462`.

[87] T.V. Vorburger, E. Marx, and T.R. Lettieri. "Regimes of surface roughness measurable with light scattering". In: *Applied Optics* 32.19 (1993), pp. 3401–3408. DOI: `10.1364/AO.32.003401`.

[88] J.W. Goodman. "Some fundamental properties of speckle*". In: *Journal of the Optical Society of America* 66.11 (1976), pp. 1145–1150. DOI: `10.1364/JOSA.66.001145`.

[89] H. Fujii, T. Asakura, and Y. Shindo. "Measurement of surface roughness properties by using image speckle contrast". In: *Journal of the Optical Society of America* 66.11 (1976), pp. 1217–1222. DOI: `10.1364/JOSA.66.001217`.

[90] Y. Ichirou, K. Koichi, and P.Y. Leonid. "Measurement of surface roughness by speckle correlation". In: *Optical Engineering* 43.11 (2004), pp. 2753–2761. DOI: `10.1117/1.1797851`.

[91] A.B. Pradana and P. Prajitno. "A Portable Surface Roughness Measurement System Using Laser Speckle Imaging Based on GLCM". In: *2019 6th International Conference on Instrumentation, Control, and Automation (ICA)*, pp. 100–105. ISBN: 2639-5045. DOI: `10.1109/ICA.2019.8916729`.

[92] D. Youssef et al. "Estimation of Articular Cartilage Surface Roughness Using Gray-Level Co-Occurrence Matrix of Laser Speckle Image". In: *Materials* 10.7 (2017), p. 714.

[93] D. Youssef, S. Hassab-Elnaby, and H. El-Ghandoor. "Nanoscale quantitative surface roughness measurement of articular cartilage using second-order statistical-based biospeckle". In: *PLOS ONE* 16.1 (2021), e0246395. DOI: `10.1371/journal.pone.0246395`.

[94] S. Saarakkala et al. "Quantification of the optical surface reflection and surface roughness of articular cartilage using optical coherence tomography". In: *Phys Med Biol* 54.22 (2009), pp. 6837–52. DOI: `10.1088/0031-9155/54/22/006`.

[95] X. Attendu et al. "Coregistered optical coherence tomography and frequency-encoded multispectral imaging for spectrally sparse color imaging". In: *J Biomed Opt* 25.3 (2019), pp. 1–12. DOI: `10.1117/1.Jbo.25.3.032008`.

[96] C.A.S.J. Gulo, A.C. Sementille, and J.M.R.S. Tavares. "Techniques of medical image processing and analysis accelerated by high-performance computing: a systematic literature review". In: *Journal of Real-Time Image Processing* 16.6 (2019), pp. 1891–1908. DOI: `10.1007/s11554-017-0734-z`.

[97] D. Evers et al. "Optical spectroscopy: current advances and future applications in cancer diagnostics and therapy". In: *Future Oncology* 8.3 (2012), pp. 307–320. DOI: `10.2217/fon.12.15`.

[98] C.-P. Liang et al. "Optical coherence tomography-guided laser marking with tethered capsule endomicroscopy in unsedated patients". In: *Biomedical Optics Express* 10.3 (2019), pp. 1207–1222. DOI: `10.1364/BOE.10.001207`.

[99] M.J. Suter et al. "Esophageal-guided biopsy with volumetric laser endomicroscopy and laser cautery marking: a pilot clinical study". In: *Gastrointestinal Endoscopy* 79.6 (2014), pp. 886–896. DOI: `https://doi.org/10.1016/j.gie.2013.11.016`.

[100] T.J. Farrell, M.S. Patterson, and B. Wilson. "A diffusion theory model of spatially resolved, steady-state diffuse reflectance for the noninvasive determination of tissue optical properties in vivo". In: *Med Phys* 19.4 (1992), pp. 879–88. DOI: `10.1118/1.596777`.